

Mechanical compaction mechanisms in the input sediments of the Sumatra Subduction Complex- insights from microstructural analysis of cores from IODP Expedition- 362

Sivaji Lahiri^{1*}, Kitty L. Milliken², Peter Vrolijk³, Guillaume Desbois¹, Janos L. Urai¹

¹Institute of Tectonics and Geodynamics, RWTH Aachen University, Germany, Lochnerstrasse 4–20, 52056, Aachen, Germany

²Bureau of Economic Geology, The University of Texas at Austin, Austin, TX, 10611, USA

³Department of Earth and Environmental Science, New Mexico Institute of Mining and Technology, 801 Leroy Place, Socorro, NM 87801, USA

* Corresponding author: sivaji.lahiri2@gmail.com

Abstract

The input sediments of the North Sumatra subduction zone margin, drilled during IODP Expedition 362, exhibit remarkable uniformity in composition and grain size over the entire thickness of the rapidly deposited Nicobar Fan succession (sea-floor to 1500 mbsf), providing a unique opportunity to study the micromechanisms of compaction. Samples were prepared from dried core samples from sites (U1480 and U1481) by both Ar-ion cross-section polishing and broad-ion beam cutting, and imaged with a field-emission Scanning Electron Microscope (SEM). Shallowest samples (sea-floor to 28mbsf) display a sharp reduction in porosity from 80% to 52% due to collapse of large clay-domain/matrix pores associated with rotation and realignment of clay-platelets parallel to the bedding plane. The deeper succession (28mbsf to 1500mbsf) exhibits less rapid reduction in porosity from 52% to 30% by the progressive collapse of silt-adjacent larger pores by bending and subsequent sliding/fracturing of clay particles. In addition, there is a correlated loss of porosity in the pores too small to be resolved by SEM.

Clastic particles show no evidence of deformation or fracturing with increasing compaction. In the phyllosilicates, there is no evidence for pressure solution or recrystallization: thus, compaction proceeds by micromechanical processes. Increase in effective stress up to 18 MPa (~1500mbsf) causes the development of a weakly aligned phyllosilicate fabric mainly defined by illite clay particles and mica grains, while the roundness of interparticle pores decreases as the pores become more elongated. We propose that bending of the phyllosilicates by intraparticle slip may be the rate-controlling mechanism.

Pore size distributions show that all pores within the compactional force chain deform, irrespective of size, with increasing compactional strain. This arises because the force chain driving pore collapse is localized primarily

31 within the volumetrically dominant and weaker clay-rich domains; pores associated with packing around isolated
32 silt particles enter into the force chain asynchronously and do not contribute preferentially to pore loss over the
33 depth range studied.

34 Introduction

35 Muds are fine-grained sediments (>50% of particles <63µm diameter) comprising platy detrital clay minerals and
36 equidimensional detrital grains such as quartz, feldspar, calcite, etc. (Nakano, 1967; Hesse, R., 1975; Sintubin,
37 1994). Understanding the mechanical, chemical, and microstructural properties of mud and mudstone is of great
38 interest for rock property prediction in basic earth science, in exploration, subsurface integrity studies and
39 geotechnical engineering (Yagiz, S., 2001; Aplin and Macquaker, 2011; Lazar et al., 2015). The chemical and
40 physical behavior of marine muds plays a critical role in defining the geometry of accretionary prisms, locating
41 the décollement for fault rupture (Vrolijk, 1990; Chester et al., 2013) and understanding subduction zone
42 earthquakes and tsunamis (Dean et al., 2010; Chester et al., 2013; Hüpers et al., 2017).

43 Marine mud is deposited with a highly porous isotropic fabric (Bowles, 1969; Bennett et al. 1981; 1991);
44 depositional porosity in mud is about twice as high as in sand (e.g., Velde, 1996, Lundegard, 1992). In contrast,
45 mudstones have low porosities, modal pore sizes measured in nm, and an absence of textural controls on porosity
46 (e.g. Aplin et al., 2006; Milliken et al., 2012; 2013). The processes in this dramatic evolution of porosity have
47 similarities to compaction of sand to sandstone, comprising a combination of compaction and cementation
48 (Milliken and Day-Stirrat, 2013), although the much smaller, elongated phyllosilicate grains increase the role of
49 clay-bound water in the process (Karaborni et al., 1996). Whereas a refined and somewhat predictive
50 understanding exists for porosity evolution in sand and sandstones (e.g., Lander and Walderhaug, 1999; Paxton et
51 al., 2002; Lander et al., 2008; Ajdukiewicz and Lander, 2010, Desbois et al., 2011), such a model is at best
52 preliminary for muds and mudstones (Pommer and Milliken, 2015; Milliken and Olson, 2017). It seems clear that
53 the composition of the grain assemblage importantly sets the stage for porosity evolution in muds (Milliken, 2014),
54 cementation being the greatest in muds with abundant biogenic debris. In contrast to sandstones, however,
55 cementation is far less common globally in mudstones (Milliken, 2019), leading to the notion that mechanical
56 compaction may be far more important in muds. In addition, depositional environment also strongly controls
57 porosity evolution, compaction and diagenesis in mudrocks (e.g. Burland, 1990; Baruch et al., 2015; Delle Piane
58 et al., 2015) as the initial clay and rigid grain compositions significantly affect both compaction (as this manuscript
59 shows) and subsequent diagenetic alteration due to variations in composition. Establishing the expected
60 compaction behavior for muds in a setting of well-constrained mud properties is an essential contribution that our
61 study hopes to serve.

62 Investigations of mud and mudstone compaction are usually based on proxy data, such as velocity or density,
63 rather than direct measurements of porosity (e.g., references in Mondol et al., 2007). Direct measurement of
64 porosity can be broadly classified into two categories: 1) laboratory experiments; (e.g., Mitchell, 1956; Bennett et
65 al. 1981; Griffiths and Joshi, 1989; 1990; Vasseur et al. 1995; Mondol et al. 2007; Fawad et al. 2010; Emmanuel
66 and Day-Stirrat, 2012), and 2) studies on natural samples (e.g., Meade, 1964; Ho et al., 1999; Aplin et al. 2003;
67 2006; Day-Stirrat et al., 2008; 2010; 2012; Milliken et al, 2012; 2013). A common shortcoming of studies on

68 natural samples is the assumption that the bulk porosity is a direct measure of compaction although porosity loss
69 has contributions of both compaction and cementation (Ehrenberg, 1989; Lundegard, 1992; Paxton et al., 2002),
70 and this can only be accomplished by petrographic inspection (Milliken and Curtis, 2016). Experimental studies
71 generally avoid this shortcoming by the use of lab-produced particle packs that undergo no chemical change during
72 the experiment. Studies of shallowly buried units (like the present study) are the ones most likely to avoid the
73 complication of cementation, especially if temperatures are low and bulk grain assemblages are siliciclastic
74 (Milliken, 2008, 2014).

75 Previous studies report contrasting ideas about the mechanisms of mechanical compaction of mud. Some studies
76 conclude that rotation is the dominant particle scale mechanism for mechanical compaction (Bowles et al., 1969;
77 Oertel and Curtis, 1972; Vasseur et al., 1995), although other particle scale-deformation mechanisms were not
78 investigated by these authors. A few studies state that burial compaction significantly increases the alignment of
79 phyllosilicate (clay and mica) parallel to the bedding planes (Bowles et al., 1969; Oertel and Curtis, 1972; Vasseur
80 et al., 1995) (a detailed review of the previous studies on mechanical compaction is given in Document S1 in
81 Supplementary data). Other studies suggest that intense mechanical compaction (i.e. effective stress) has a limited
82 impact on the development of phyllosilicate fabric in mud (Ho et al., 1999; Aplin et al., 2006; Day-Stirrat et al.,
83 2008; 2011). In addition, earlier authors concluded that an increase in effective stress causes preferential loss of
84 larger pores, and as a result, the mean porosity of the samples decreases (Delage and Lefebvre, 1884; Griffiths and
85 Joshi, 1989; 1990; Emmanuel and Day-Stirrat, 2012). With increasing consolidation stress, a bimodal pore size
86 distribution curve shifts toward smaller pore sizes as larger pores rapidly collapse (Griffiths and Joshi, 1989; 1990;
87 1991). These studies investigated the changes in particle alignment and reduction in porosity (Ho et al., 1999;
88 Aplin et al., 2006; Day-Stirrat et al., 2008; 2011) but without imaging the evolution of pore morphology with
89 increasing compactional strain. Moreover, in previous studies, the authors mainly performed laboratory
90 consolidation experiments on lab produced particle packs, and used conventional techniques, such as mercury
91 intrusion porosimetry and high-resolution X-Ray pole figure goniometry (HRXTG) to understand the evolution of
92 pore size distribution with consolidation stress (Ho et al., 1999; Aplin et al., 2006). Studies on naturally compacted
93 samples are rare.

94 We received 55 mud samples from drill cores collected during IODP Expedition 362 west of the North Sumatra
95 subduction zone margin and investigated the evolution of petrographic microstructure and pore morphology as a
96 function of compactional strain. Apart from general implications for global mudrocks, we hope this investigation
97 will also contribute to studies that seek to predict rock properties in the deeper subsurface at the Sumatra
98 subduction front.

99

100 Geological background and drilling

101 The Sumatra subduction zone extends 5000km from the Andaman-Nicobar Islands in the northwest to the Java-
102 Banda arc in the Southeast (Fig.1a and b) (Prawirodirdjo et al., 1997; Hippchen and Hyndman, 2008). The trench

103 of the Sumatra subduction zone (Fig.1a) developed on the subducting Indo-Australian Plate at a convergence rate
104 of 5.5 cm/yr in the north and 7.23 cm/yr in the South (Ghosal et al., 2014; Moeremans, and Singh, 2015).

105 On 26th December 2004, the west coast of Northern Sumatra recorded one of the largest earthquakes (Mw-9.3) in
106 the 21st century, generating a devastating Tsunami in the Indian Ocean (Ammon et al., 2005; Lay et al., 2005).
107 Understanding the mechanism(s) behind this unprecedented event was the central idea behind IODP Expedition
108 362 (Fig.1). The main objective of the expedition was to collect core and log data of the incoming sedimentary
109 succession of the Indo-Australian oceanic plate to understand the seismogenic process related to the margin (Dugan
110 et al., 2017; McNeill et al., 2017). During the expedition in 2016, drilling was performed on two sites: U1480
111 (Holes E, F, G and H) and U1481 (Hole A) located on the oceanic plate west of the North Sumatra subduction
112 margin and east of the Ninety East Ridge (Fig.1a, b) (Dugan et al., 2017). The drilling sites recovered a complete,
113 1.5 km thick sedimentary section from late Cretaceous to Pleistocene down to the basement of basaltic crust
114 (Dugan et al., 2017; McNeill et al., 2017).

115 The input sedimentary section of the Sumatra subduction zone comprises the distal part of the trench wedge,
116 Nicobar fan sequence, and pre-fan pelagic section on the basaltic crust at the bottom (Dugan et al., 2017; McNeill
117 et al., 2017). At Site U1480, the entire recovered section was categorized into six lithological entities, Units I to
118 VI (Fig. 1c) (McNeill et al., 2017). Unit I (0 to 26.72 mbsf) consists of unconsolidated calcareous clay, silty clay
119 with alternating fine sand (McNeill et al., 2017). Unit II from 26.72 to 1250 mbsf consists of three subunits (IIA,
120 IIB and IIC) and mainly exhibits alternating fine-grained sand and silty clay to silt (McNeill et al., 2017). Unit III
121 (1250 ~ 1327 mbsf) is divided into two subunits: Unit IIIA and IIIB (McNeill et al., 2017). Unit IIIA consist of
122 thin to medium-bedded, gray-green or brown mudstone and intercalated siltstone, and Unit IIIB is composed of
123 reddish-brown tuffaceous silty claystone with fragmented sponge spicules and radiolaria (McNeill et al., 2017).
124 The boundary between Units IIIA and IIIB (1310 mbsf) at this site marks the base of the Nicobar Fan and the
125 beginning of the thin pre-fan succession (Pickering et al., 2020). Units IV, V, and VI include volcanoclastic rocks
126 with tuffaceous sandstone, conglomerates, and basaltic oceanic crust, respectively. At Site U1481, the pre-fan
127 succession was not encountered and a Unit III, a thicker equivalent of Subunit IIIA at Site U1480, represents the
128 material of the lower Nicobar Fan (see Figure F15, in Site U1481 report; McNeil et al., 2017). This study is
129 restricted to the thin, distal trench wedge (Unit I) and Nicobar fan sequence (Units II and IIIA, which is equivalent
130 to Unit-III at U1481).

131 X-ray diffraction (XRD) of bulk samples and clay fractions at Site U1480 show a clay mineral assemblage
132 dominated by illite with lesser amounts of smectite and chlorite (Rosenberger et al., 2020) (Fig.2a, b, c and d;
133 Table S1 and Figure S1 in Supplementary data). Siliciclastic samples consist of 50-70% clay (McNeill et al.,
134 2017). Smectite is more abundant in Unit I than Unit II, where smectite abundance ranges from 5-30% with rare
135 samples containing as much as 45% smectite. In Unit II, smectite fraction ranges from 10-30% with local
136 enrichments as great as 40-45%. Smectite again increases in Unit III, reaching a value as high as 68% in the
137 samples attributed to the Nicobar Fan section. There is a weak increase in the expandability of mixed-layer I/S
138 with depth (Rosenberger et al., 2020) (Figure-S2 in Supplementary data), and there is no change in the amount of
139 illite in mixed-layer I/S (ca. 20% illite). Montmorillonite is interpreted as the smectite mineral (Rosenberger et
140 al., 2020). Chlorite + kaolinite abundance is similar in Units I and II, ranging from 8 to 20% with rare occurrences

141 as high as 24%; Unit III is almost devoid of chlorite + kaolinite. Heating experiments on select samples indicate
142 that chlorite makes up 66-100% of this mineral category (Rosenberger et al., 2020). Illite comprises the remainder
143 of the clay mineral assemblage, ranging from 50-79% in Unit II while Unit I is correspondingly less illite-rich (42-
144 70%). In the Unit III Nicobar Fan section, illite makes up only 18-36% of the clay fraction.

145 The Nicobar fan sequence exhibits almost compositionally homogeneous (silt/clay ratio; mostly 'silty-clay')
146 subunits with uniform grain size (McNeill et al., 2017), and a history of rapid deposition (125-290 m/my; Backman
147 et al., 2019). The sedimentary sequence exhibits no evidence of uplift and currently occurs at maximum burial
148 depth. The drilling sites are 255 km away from the deformation front; thus the samples are undisturbed by tectonic
149 faulting associated with subduction (Fig.1b). In addition, owing to the scarcity of biogenic grains and the low
150 temperatures encountered (<68°C), cementation is only observed as highly localized concretions (Red colored
151 symbols in Fig.2e, f, g, and h) (McNeil et al., 2017; Torres et al., 2022). Such a homogeneous sedimentary
152 succession extending across 1.5 km depth is rare in sedimentary basins. Hence, these samples provide us with a
153 unique opportunity to study depth-wise variation in microstructure as a function of vertical effective stress with
154 few complications from multiple causes of porosity loss.

155 Sampling and Methods

156 This study is based on two sample sets that were obtained from Sites 1480 (Holes E, F, G, and H) and 1481 (Hole
157 A) independently and analyzed by slightly different methods. The first sample set (33 mud samples; depth 1.24 to
158 1300 mbsf) was prepared using Broad Ion Beam polishing and analyzed using Scanning Electron Microscope
159 (BIB-SEM technique) at RWTH Aachen University, Germany. The second sample set (22 samples; depths 6.25
160 to 1493.30 mbsf) was prepared using Ar-ion cross-section polishing and imaged by field-emission SEM at the
161 Bureau of Economic Geology (BEG) at the University of Texas at Austin. Respective core description of these
162 55 mud samples and their bulk mineralogy data are tabulated in Table-1.

163 BIB-SEM technique (First set of samples, Aachen University)

164 Sample preparation for BIB-SEM and imaging

165 After drilling, the samples were stored at Kochi drill core repository (IODP), Japan for four years (2016 ~ 2020)
166 at the refrigerated storage areas maintaining the temperature of ca. 4°C and 80% humidity (http://www.kochi-core.jp/en/iodp-curation/curation-sop_2.html). We received a total of 33 freeze-dried mud samples (SN-1 to SN-
167 33 in Table-1) for analysis at Aachen. The samples were collected using a tube inserted perpendicular to the cut
168 face of the drill core in such a way that the notch of the tube identified the top of the sample so the orientation of
169 bedding planes for each sample was known. In Fig. 1d, a tube sample received from the IODP repository is shown,
170 where the red line on the top of the tube identifies the notch. Subsamples (10 x 5 x 2 mm³) were cut from the
171 individual freeze-dried samples using a razor blade. These subsamples were pre-polished using silicon carbide
172 (SiC) paper to reduce the roughness of the surface down to 10 µm. Further, Broad Ion Beam (BIB) polishing was
173 carried out using a JEOL SM-09010 cross-section polisher for 10 hours at 6 kV and 150 µA. BIB reduces surface
174 damage by removing a 100 µm thick layer to generate a high-quality polished cross-section of 1-2 mm² with a
175 topography less than 5 nm (Desbois et al., 2009).
176

177 After polishing, the BIB cross-sections were coated with tungsten and imaged with a Zeiss Supra 55 SEM with
178 SE2, BSE, and EDX detector (Figure S3 in Supplementary data). SE2 images were used to image porosity and
179 BSE images are combined with an EDX map as well as EDX point analysis for identifying mineral phases. For
180 each cross-section, we made mosaics of hundreds of SE2 and BSE images at a magnification of 20,000x (~14.3
181 nm pixel value) and 10,000x respectively, with an overlap of 20% to 30%, (Klaver et al., 2012; 2015; 2016; Hemes
182 et al., 2013; 2015; 2016; Laurich et al., 2014). The mosaics are stitched together using Aztec software preserving
183 the original pixel resolution. Finally, these stitched images are used for the segmentation of pore spaces, minerals,
184 and other respective analyses.

185 Image segmentation and pore analysis

186 For quantifying porosity and pore morphology, individual SE2 image mosaics were segmented using a ‘seed and
187 grow’ algorithm (Adams and Bischof, 1994) implemented with a MatLab code (Jiang et al., 2015; Schmatz et al.,
188 2017) (Figure S3 in Supplementary data). The ‘seed and grow’ algorithm works based on the difference in intensity
189 of greyscale value in an image (bright = minerals, dark = pores). After automatic segmentation, individual pores in
190 SE2 images are manually corrected if required.

191 Similarly, using ImageJ software (threshold toolbox and machine learning algorithm), segmentation of the
192 individual mineral phases was carried out combining BSE images and EDX elemental maps. While quartz, calcite,
193 pyrite, mica minerals are efficiently segmented using these tools, feldspars are found difficult to segment because
194 of similar composition as clay (Figure S4, S5 and S6 in Supplementary data). Finally, corrected pore segmented
195 SE2 mosaics are overlaid on the phase maps using the ‘georeference’ tool of QGIS (<http://qgis.osgeo.org>), (Figure
196 S4, S5 and S6 in Supplementary data).

197 Pore detection resolution (PPR) and representative area analysis (REA)

198 ‘Practical pore detection resolution’ (PPR) indicates the pore sizes above which one can assume to detect 100% of
199 the pores present in the SE2 mosaic (Klaver et al., 2012). In agreement with earlier results using this instrument
200 (Klaver et al., 2012; 2015; 2016; Hemes et al., 2013; 2015; 2016; Laurich et al., 2014), we found PPR of ~2000
201 nm² and ~8500 nm² for the magnification of 20,000x and 10,000x images, respectively, corresponding to 10 pixels.

202 After segmenting all minerals, representative elementary area analysis (REA) was performed using the box
203 counting technique on mineralogical phase maps (Kameda et al., 2006; Klaver et al., 2012). Similar steps are also
204 followed for determining a representative elementary area for SE2 images. The estimated REA values using SE2
205 and BSE mosaics for the analyzed 33 mudstone samples are documented in Table S2 in Supplementary data.

206 Porosity, pore morphology, pore size, and the statistical distribution of pores were obtained using image analysis
207 techniques on 2D images collected using BIB-SEM technique. Because pores are non-spherical 3D objects that
208 are cut perpendicular to the bedding plane to acquire a 2D image dataset, there may be random and systematic
209 errors when comparing 2D and 3D results. We plotted shipboard measured MAD (moisture and density) porosity
210 vs depth (Fig.2e) and also BIB-SEM porosity vs depth for the analyzed samples (Fig.3a), where MAD porosity
211 documents bulk porosity for the sample, and BIB-SEM porosity represents 2D cuts of the non-spherical 3D

212 pores/porosity. Because there is first-order correspondence between the two porosity measurements, we deduce
213 that porosity and pore size distributions obtained from 2D image analysis reflect the bulk rock porosity and 3D
214 pore size distribution of the samples. In addition, the estimated REA appears appropriate for minimizing systematic
215 errors in the bulk pore characteristics of the sample.

216

217 Ion polishing and SEM technique (second set of samples; BEG, UT Austin).

218 22 Samples (SN-34 to SN-55 in Table 1) were taken shipboard from the sample half of the still-wet core in small
219 plastic tubes (similar to the ones used for the sample set at Aachen) inserted into the core by manual pressure. The
220 tubes were removed from the core and sealed in plastic bags. In the laboratory at the BEG, sample bags were
221 opened, and the muds were allowed to dry slowly in the tubes over several weeks. No discernible shrinkage was
222 observed as the dried core pieces still fully filled the tubes. The tubes were carefully removed, and a small cube
223 (approximately 0.5 to 1 cm³) was cut using a sharp knife and small hand saws; an orientation mark was placed on
224 the cube to indicate the bedding direction. Bed-perpendicular surfaces were prepared by Ar-ion cross-section
225 polishing, using the Leica EM TIC020 triple ion beam miller and coated with Ir for imaging. Manual placement
226 of the cut cubes into the ion mill is not precise so the ion-polished surfaces have slight variation from perpendicular
227 to bedding. Pore imaging was performed on the FEI Nova NanoSEM 430 using the in-lens SE detector, a 30 μm
228 aperture, 15 KeV accelerating current, a working distance of around 5–6 mm, and an intermediate-range sample
229 current (spot size = 3, mid-range for the instrument). Randomly selected views (typically 3-6) of all samples were
230 collected at 6kx machine magnification; additional views illustrating pore types and pore/grain relationships were
231 made at 10kx to 30kx (machine magnification).

232

233 Results

234 Compaction strain derived from MAD-porosity data

235 During Expedition 362 mass and volume of mud samples were measured in both wet and dry states using a high
236 precision electronic mass balance and helium pycnometer (http://www-odp.tamu.edu/publications/tnotes/tn37/tn37_8.htm). Using the obtained mass and volume dataset for wet and dry conditions, bulk MAD (moisture and
237 density) porosities were calculated. Porosity values reported by McNeill et al. (2017) and downloaded from IODP
238 databases serve as the basis for strain calculations.

240 Shipboard MAD porosity for mud samples exhibits a sharp reduction from 80% to 52% from the seafloor to 28
241 mbsf (Fig.2e). Deeper samples display a comparatively smaller reduction in porosity of approximately from 52%
242 to 30% over a depth range of 28 to 1500 mbsf (Fig.2e and f).

243 We calculated compaction strain following a method proposed by Nollet et al. (2005) and subsequently used by
244 Neagu et al. (2010) (Fig.2g and h), assuming 1D consolidation and no change in solid volume. The compaction
245 strain (ϵ_c) is then computed as:

$$246 \quad \epsilon_c = \frac{1-\phi_0}{1-\phi_1} \quad (\text{Eqn-1})$$

247 Here ϕ_0 = initial porosity, and ϕ_1 = final porosity. Samples from sites U1480 and U1481 show no evidence of
248 tectonic faults (McNeill et al., 2017), supporting an assumption of 1D strain. We considered the initial porosity ϕ_0
249 as the MAD porosity at 0.6 mbsf depth ($\phi_0 = 80\%$). Compaction strain following Eqn-1 (Table S2 in
250 Supplementary data), is plotted against depth in Fig.2g and h. Compaction strain increases from 1 to 2.05 from the
251 seafloor to 28 mbsf (i.e. Unit I), and from 2.00 to 3.05 from 28mbsf to 1500 mbsf (Fig. 2g and h).

252 Another common measure of compaction is the intergranular volume (IGV; Paxton et al., 2002), which
253 corresponds to the sum of intergranular porosity and intergranular cement. In some mudstones, it may be necessary
254 to calculate IGV differently because of the presence of abundant primary intragranular pores and pore-filling
255 bitumen (Milliken and Olson, 2017). In our sample set, cement is absent, and IGV is taken to equal the bulk
256 porosity from shipboard MAD measurements.

257 Compactional porosity loss (COPL), referenced against the original sediment volume, is calculated from the initial
258 primary intergranular porosity (P_i ; 80% in this case) and the IGV as follows (Ehrenberg, 1989, Lundegard, 1992):

$$259 \quad \text{COPL} = P_i - ((100 - P_i) \times \text{IGV}) / (100 - \text{IGV}) \quad (\text{Eqn-2})$$

260 At an IGV of 50%, COPL is 60%; in the deepest samples in the Nicobar fan (IGV of around 30%) COPL is 70%
261 (Table S2 in Supplementary data).

262 Description of grain microstructure and pore morphology

263 To have consistency in the data set, we prepared SE2 mosaics for all samples from the Aachen sample set at
264 20,000x magnification covering an average $100 \times 100 \mu\text{m}^2$ area. In addition, to examine the effect of magnification
265 on BIB-SEM porosity and representative area analysis (REA), three samples (i.e. SN-7, SN-15, and SN-29) were
266 also imaged each at 5,000x and 10,000x magnification, respectively. A decrease in magnification and resolution
267 reduces visible BIB-SEM porosity.

268 We observed consistent results for the REA analysis. For SE2 mosaics, REA varies between $45 \times 45 \mu\text{m}^2$ to 85×85
269 μm^2 at 20,000x magnification, and for segmented phase maps, REA varies between $90 \times 90 \mu\text{m}^2$ to $130 \times 130 \mu\text{m}^2$
270 at 10,000x magnification. In the UT sample set, the standard images taken at 6kx with machine magnification are
271 $49.7 \times 45.7 \mu\text{m}^2$, so these images are also within the estimated REA range.

272 Based on EDX elemental map or point analysis, six mineral phases occur in significant amounts in the Sumatra
273 samples: Quartz, feldspar (K-feldspar, Na-feldspar), calcite, pyrite, micas (muscovite, biotite, and chlorite), and

274 clay. Based on XRD analyses (Rosenberger et al., 2020), the clay size fraction is dominated by illite. Clay + mica
275 percentage in these mudstone samples varies between 65% to 75%. Samples SN-1 (77%) and SN-4 (76%) have
276 more clay + mica, whereas SN-7, SN-9, SN-17, SN-28, SN-29, and SN-31 contain less clay + mica (<65%) (Table
277 S2 in Supplementary data).

278 Using BIB-SEM and automatic pore segmentation techniques, an average of >30,000 pores have been detected
279 for each individual sample in the Aachen sample set at 20,000x magnification. Correlating with the MAD data set,
280 the estimated BIB-SEM porosity reduces from 32% to 19% over a depth range of seafloor to 28 mbsf, while the
281 deeper samples display a smaller reduction from 19% to 10% over a depth range of 28 to 1500 mbsf respectively
282 (Fig.3a). Consistent with numerous previous studies, the results document a mismatch between bulk measured
283 porosity (MAD) and imaging porosity (BIB-SEM) (e.g., Hemes et al., 2013; Houben et al., 2014; Nole et al., 2016;
284 Oelker et al., 2019) (Table S2 in Supplementary data). We plotted BIB-SEM porosity vs MAD porosity and found
285 an approximately linear correlation with coefficient of determination ($R^2 = 0.8621$) (Fig. 3b).

286 Type of pores

287 Intergranular pores contribute >99% of the total visible porosity. Intragranular pores (see below) are rare. The size
288 and shape of intergranular pores change during compaction (Table S3 in Supplementary data).

289 Intergranular pores are classified (Fig.4) based on the size of surrounding particles (irrespective of mineralogy):
290 1) Clay domain (matrix) pores, and 2) silt-adjacent pores. Based on the variation in size, clay domain pores are
291 divided further into: 1) Large clay domain pores (pore size $>5 \times 10^5 \text{ nm}^2$) and the pore boundary is defined by more
292 than three clay particles; and 2) small clay domain pores (pore size $<5 \times 10^5 \text{ nm}^2$) that occur between 2-3 clay
293 particles (see further details below). Large and small clay domain pores are classified by geometry as: 1) Elongate
294 pores (aspect ratio $>3:1$) and 2) equant-shaped pores (aspect ratio $<3:1$). Elongate pores consist of 1) Linear-
295 elongated pores, and 2) crescent-shaped elongated pores. Examples of different clay-domain pore types are shown
296 in Fig. 5, 6, and 7.

297 Silt-adjacent pores are categorized by two types: 1) large silt-adjacent pores are $>5 \times 10^5 \text{ nm}^2$, and pore boundaries
298 are defined by more than three particles; and 2) small silt-adjacent pores include pore sizes $<5 \times 10^5 \text{ nm}^2$, and pore
299 boundaries are defined by two/three particles (see further detail on the modal sizes of these pore types below).
300 Large and small silt-adjacent pores are either: 1) Equant shaped (aspect ratio $<3:1$) or 2) elongated (aspect ratio
301 $>3:1$). Further, elongated silt-adjacent pores consist of 1) linear-shaped elongated pores and 2) crescent-shaped
302 elongated pores. These pore types are highlighted in Fig. 5, 6, and 7.

303 Change in inter-particle pore morphology with depth

304 Seafloor to 28mbsf (Unit I)

305 The shallow mud samples in Unit I are unconsolidated and porous (Fig. 5a). Sample SN-1 (1.24 mbsf) has a
306 maximum MAD porosity of 80%. We observe three types of clay particle contacts in the microstructure of SN-1;
307 edge to edge (EE), edge to face (EF), and face to face (FF) contacts (Table S4 in Supplementary data). Among
308 them, EF and FF contacts are abundant and EE contacts are rare. The sample exhibits abundant large clay domain

309 pores and large silt-adjacent pores that are equant with smooth edges and a rounded pore perimeter. The sample
310 also contains abundant linear-elongated and equant-shaped small clay-domain pores. Crescent-shaped small clay
311 domain pores are rare in the microstructure of this sample. Equant-shaped, small silt-adjacent pores are abundant.
312 In addition, linear elongated and crescent-shaped small, silt-adjacent pores are also common (Fig.5a; [Table S3 in](#)
313 [Supplementary data](#)).

314 With increasing compaction strain ($\epsilon_c = 1.119$) and depth (5.1 mbsf; [Figure S7 in Supplementary data](#)), porosity
315 (MAD) reduces to 75% and corresponding COPL=19% (sample SN-2; Fig. 5b, [Table S2 in Supplementary data](#)).
316 The microstructures of SN-2 display are similar characteristics to those observed in sample SN-1, although there
317 are fewer large clay domain pores in SN-2 than SN-1. Linear elongated and equant-shaped small clay domain
318 pores are common [Table S3 in Supplementary data](#), but crescent-shaped small clay domain pores are rare. The
319 microstructures of SN-2 exhibit abundant equant-shaped large and small silt-adjacent pores.

320 With an increase in compaction strain to $\epsilon_c \sim 2.00$ (28 mbsf), the sample microstructure is dominated by FF contacts
321 (Fig. 5c), and EE and EF contacts are rare [Table S4 in Supplementary data](#). Additionally, large clay-domain pores
322 become infrequent in the microstructure (Fig. 8). Crescent-shaped, small clay domain pores in the microstructure
323 are rare, whereas equant-shaped small clay domain pores are common. Both small and large silt-adjacent pores
324 exhibit equant shapes (Fig. 8d, e and f). The sample analyzed at the base of Unit I (SN-6; 28 mbsf) contains rare
325 large clay-domain pores and abundant FF contacts (Fig. 5c; MAD porosity = 54% and COPL = 55%).

326 *28 mbsf to 1500 mbsf (Units II and III)*

327 Mud samples from the Nicobar fan section are more compacted than shallower samples. We analyzed a total of 29
328 samples using BIB-SEM at Aachen and 18 samples using the field emission SEM at UT Austin from this section.
329 An increase in compactional strain from 2.00 to 3.15 over a depth range of 28 to 1500 mbsf causes a porosity
330 reduction (MAD) of 54% to 28%, and the corresponding change in average COPL is 55% to 72%. The
331 microstructure of these samples is dominated by FF contacts among clay particles; EF and EE contacts are rare
332 ([Table S4 in Supplementary data](#); Fig. 6 and 7 b, c). All samples exhibit abundant small linear-elongated clay
333 domain pores between two parallel clay sheets (Fig. 8b). Equant-shaped small, clay domain pores are rarely
334 observed below 150 mbsf depth ($\epsilon_c > 2.4$). Crescent-shaped, small, clay domain pores are rare at shallow depth but
335 become abundant with an increase in compactional strain $\epsilon_c > 2.95$ (871.87 mbsf) as the surrounding clay particles
336 are bent (Fig.6). In addition, large clay domain pores in these samples are rarely observed in the vicinity of silt
337 clasts (Fig.6, [Figure S8 in Supplementary data](#)).

338 Below 100 mbsf ($\epsilon_c = 2.20$), silt-adjacent small pores are dominantly equant shaped, but below 300 mbsf ($\epsilon_c > 2.5$)
339 silt-adjacent small pores are dominantly linear-elongated (Fig. 8e). Crescent-shaped, small, silt-adjacent pores are
340 common in all samples. Large silt-adjacent pores are dominantly equant above 200 mbsf depth ($\epsilon_c < 2.40$) and
341 commonly linear-elongate below 400 mbsf depth ($\epsilon_c > 2.5$) (Fig.8f). It appears that due to an increase in
342 compactional strain the shape of the silt-adjacent pores changes from equant to linear-elongated ([Table S3 in](#)
343 [Supplementary data](#)). In samples with more silt, equant-shaped small and large, silt-adjacent pores can persist at
344 greater depths (Fig. 8e and f).

345 Below 28 mbsf ($\epsilon_c > 2.0$), the number of large silt-adjacent pores in the microstructures decreases. Comparing
346 samples SN-8 (74.07 mbsf and $\epsilon_c = 2.09$) and SN-32 (1267.14 mbsf and $\epsilon_c = 3.15$) illustrates how the number of
347 large, silt-adjacent pores decreases with depth (Fig. 6a, and c) when the clay fraction (Table S2 in Supplementary
348 data) is comparable. This relationship is apparent even in samples separated by a smaller depth difference (SN-
349 49 from 959.14 mbsf and SN-55 from 1433.36 mbsf; Fig. 7b and c). While the number of large pores diminishes,
350 the maximum size of the large silt-adjacent pores remains constant (10^7 nm^2 ; Figure S9).

351 Variation in the orientation of pores and grains due to compactional strain

352 We examined the change in orientation of the long axis of pores with increasing compaction strain. For all
353 segmented pores, the angle between the long axis and the bedding plane was determined and plotted in rose
354 diagrams (Supplementary data-15). Samples from the seafloor to 28 mbsf exhibit a weak preferred orientation of
355 the long axis of pores with maxima oriented obliquely to the bedding planes. However, below 28 mbsf the samples
356 have a preferred orientation of the long axis of pores aligned subparallel to the bedding plane. Further, due to an
357 increase in vertical effective stress down section below 28 mbsf in Units II and III, the degree of preferred
358 alignment of the long axis of pores only increases to a small amount (Figure S10).

359 We determined the angle between the long axis of individual silt grains and the bedding plane for all samples and
360 plotted the angle in a rose diagram (Figure S10). For quartz, feldspar, and calcite the degree of preferred orientation
361 of the long axis of grains changes little with depth. However, the rose diagrams obtained for mica show weak
362 maxima parallel to the bedding plane and several submaxima oriented obliquely to the bedding plane above 28
363 mbsf. Preferred alignment of the long axis of mica grains increases at 28 mbsf with a strong maximum oriented
364 parallel to bedding plane. Below 28 mbsf, further increase in the degree of preferred alignment is small.

365 Size distribution of pores

366 Pore size distributions (Fig. 9) of shallow samples (Unit I) are trimodal. Sample SN-1 has peaks between 10^5 to
367 10^6 nm^2 , 10^6 to 10^7 nm^2 , and 10^7 to 10^8 nm^2 , and SN-2 has peaks from 10^4 to 10^5 nm^2 , 10^5 to 10^6 nm^2 , and 10^6 to
368 10^7 nm^2 . These three pore size regimes correspond to the small clay domain and silt-adjacent pores, large clay
369 domain pores, and large silt-adjacent pores. Samples of Units II and III exhibit bimodal pore size distributions
370 (SN-10, SN-26, and SN-33 in Fig. 9). SN-10 has a peak between 10^5 to 10^6 nm^2 , corresponding to small clay
371 domain and silt-adjacent pores, and 10^6 to 10^7 nm^2 , reflecting large silt-adjacent pores. Large clay domain pores
372 are absent from samples below 28 mbsf depth (Units II and III) based on the pore size distributions combined with
373 image analysis. At shallow depths, the contribution to total porosity by larger silt-adjacent pores is greater
374 compared to the contribution by small clay domain pores (Fig. 9e and g). The contribution of large, silt-adjacent
375 pores to total porosity diminishes with depth. Hence, at greater depth, contribution to total porosity by larger silt
376 adjacent pore is less compared to small clay domain pores (Fig. 9i).

377 Pore size distributions follow a power-law shown on a double logarithmic graph following the equations (Klaver
378 et al., 2012; 2015; 2016; Hemes et al., 2013; 2015; 2016; Laurich et al., 2014):

$$379 \quad \frac{N_i}{b_i S_{mosaic}} = C S_{pore}^D \quad (\text{Eqn-3})$$

$$380 \quad \log\left(\frac{N_i}{b_i S_{mosaic}}\right) = -D \cdot \log(S_{pore}) + \text{Log } C \quad (\text{Eqn-4})$$

381 Where N_i = number of pores with area S_{pore} , b_i = bin size, S_{mosaic} = surface area of the current mosaic, C =constant,
 382 and D = power-law exponent. The resulting power-law exponent (D) varies between 1.70 to 2.00 (Table T2 in
 383 Supplementary data).

384 Effect of texture on porosity, pore morphology, and orientation of pores

385 We analyzed six samples (SN-7, SN-9, SN-17, SN-28, SN-29, and SN-31) that are enriched in silt content
 386 compared to the rest of the mud samples (Table T2 in Supplementary data). Silt content has a positive correlation
 387 to the total SEM porosity. For example, sample SN-29 (1172.88 mbsf) exhibits a BIB-SEM porosity of 14%
 388 whereas other samples from a similar depth with less silt exhibit an average BIB-SEM porosity of 12% (Table T2
 389 in Supplementary data) at 20000x magnification. The samples with greater silt content are also enriched in equant-
 390 shaped silt-adjacent larger pores (Fig.10a). We also estimated the orientation of the long axis of pores for these
 391 three samples and plotted the obtained results as rose diagrams (Fig.10b). The obtained results exhibit a relatively
 392 weak preferred alignment of the long axis of pores with respect to the bedding planes (Fig.10b).

393

394 Discussions

395 Effective stress vs porosity: A comparison with experimental study

396 To understand the consolidation mechanisms of the Sumatra sediments, we estimated vertical effective stress
 397 following the steps proposed by Hüpers et al. (2015). Following Terzaghi and Peck (1948) vertical effective stress
 398 (σ_v') is expressed as:

$$399 \quad \sigma_v' = \sigma_v - P_f \quad (\text{Eqn-5})$$

400 Here σ_v = total vertical stress caused by the overburden load, and P_f = fluid pressure. To compute vertical effective
 401 stress of a layered sediment, we use Eqn 6:

$$402 \quad \sigma_v' = \sum(\rho_s - \rho_w) \cdot g \cdot \Delta z \quad (\text{Eqn-6})$$

403 where ρ_s = bulk density of the sediment, ρ_w = density of the pore water, Δz = depth interval, and g = gravitational
 404 acceleration. Although small offset strike-slip faults are evident at the seafloor and in seismic reflection profiles
 405 (McNeill et al., 2017), the amount of strain attributed to these fault offsets supports the idea that the maximum
 406 horizontal stress is comparable to the vertical stress; there is no evidence in seismic reflection data or from core
 407 microstructures for thrust or reverse faults associated with a vertical least principal stress. On this basis, we assume
 408 that vertical stress is the maximum principal stress, and that pore pressure is hydrostatic. Bulk density of the

409 sediment ρ_s was acquired from MAD data set obtained from IODP website (McNeill et al., 2017), and ρ_w was
410 considered as the density of seawater i.e. 1025 kg/m³ (Hüpers et al., 2015).

411 We plotted vertical effective stress against MAD porosity for 55 mud samples (Fig.11). Fawad et al. (2010)
412 experimentally studied the consolidation behavior of mud with varied proportions of silt and clay. While Sumatra
413 samples follow trends like those defined by Fawad et al. (2010), the experimental samples are more compacted
414 than natural Sumatra samples for the same silt content.

415 Clay mineralogy has a significant effect on the compaction behavior of mudstone (Mondol et al., 2007). Mondol
416 et al. (2007) performed compaction experiments using pure smectite and pure kaolinite clay particle packs because
417 they represent two end members compared to other clay minerals (illite and chlorite) in terms of grain size and
418 surface area. Smectite is the more fine-grained clay with the largest surface area while kaolinite is coarser and has
419 a smaller surface area than other clay mineral types (Meade, 1964; Mesri and Olson, 1971; Rieke and Chilingarian,
420 1974). Kaolinite is more compressible than smectite, and clay compaction gradually decreases with increasing the
421 proportion of small size clay particles in the sample (Mondol et al, 2007).

422 Fawad et al., (2010) used clay mixtures of 81% kaolinite, 14% mica, and 5% microcline grains, whereas Sumatra
423 mud samples are composed of 50%-79% illite and 5%-30% smectite, with only 8-20% undifferentiated chlorite
424 and kaolinite and 5-10% quartz particles. Therefore, due to higher illite and smectite content, Sumatra muds
425 appeared to be less compacted than the experimental samples used by Fawad et al. (2010).

426 BIB-SEM porosity vs MAD porosity

427 We note that BIB-SEM porosity is lower than the porosity found from shipboard MAD data, however the two
428 measurements correlate along a line through the origin. (Fig.3b). The reason for this difference is that MAD
429 porosity measures the total amount of moisture in a much larger sample and accounts for pores much below the
430 PPR. Rare large pores are also under-represented in the 1 mm² BIB section. Earlier studies also documented and
431 discussed mismatches between MAD and BIB-SEM measurements (Hemes et al., 2013; Houben et al., 2014; Nole
432 et al., 2016; Oelker et al., 2019). We plotted estimated BIB-SEM porosity and MAD porosity data from earlier
433 studies on Boom clay (Hemes et al., 2013; Oelker et al., 2019); Opalinus clay (Houben et al., 2014) and samples
434 from the Nankai trough (Nole et al., 2016). The data for Boom clay and Opalinus clay follow a similar trend to the
435 Sumatra samples, whereas clay samples from the Nankai trough shows a different trend. This difference may be
436 attributed to differences in magnification of Nankai trough samples.

437 In addition, we plotted clay content against the difference between the two porosities in Fig.12a. We performed
438 regression analysis using the data set for the 33 mud samples analyzed at Aachen (Fig.12b) for BIB-SEM porosity
439 versus MAD porosity (following Eqn-7) but also incorporating the effect of clay content (following the Eqn-8).

$$440 \text{ BIB-SEM porosity} = a * \text{MAD porosity} + c \quad (\text{Eqn-7})$$

$$441 \text{ BIB-SEM porosity} = a * \text{MAD porosity} + b * \text{clay content} + c \quad (\text{Eqn-8})$$

442 The coefficient of determinations (R^2) for Eqn-7 and Eqn-8 are 0.8408 and 0.9262 respectively. These results
443 suggest that the ratio in porosity depends on depth and clay content.

444 For all samples the BIB-SEM pore size distribution follows a power-law over an interval of three orders of
445 magnitude. We may extrapolate this below the practical pore resolution (PPR; Klaver et al., 2012; Kuila and
446 Prasad, 2013; Wang et al., 2019). Extrapolating our data set down to 3nm pore diameter, the BIB-SEM porosity
447 increases only up to 20%~25%. A mismatch of 15% to 20% between the MAD porosity and extrapolated BIB-
448 SEM porosity remains. The fall -off from the normal trend in log-log pore size distribution plots (Fig.9b) for the
449 shallow depth (Unit-I) samples suggest that also large pores are also under-counted in the data set. The mud
450 samples from Unit-I contains forams that are rare or absent in the deeper section (Figure S11 a, b, c, and d in
451 Supplementary data), and part of missing pore volume can be attributed to the intact forams that may be missed
452 due to the small size of the BIB SEM sample.

453 Another factor that can create a mismatch between data sets is drying artefacts. In the past, Desbois et al. (2014)
454 performed a detailed study on drying artefacts of mudstone samples using Cryogenic BIB-SEM technique. They
455 identified four types of drying damages (Type-I, II, III and IV) that can develop during drying of a mudstone.
456 Type-I and type-II drying damage develops at clay/clay particle interfaces with tip to long axis contact, and at
457 clay/clast interfaces. Heterogeneous deformational behavior or shrinkage strain of clay and/or non-clay mineral
458 grains can cause a build-up in stress at the boundary between particles during drying. Type-III drying artefacts are
459 large cracks that develops within the clay matrix itself. Type-IV drying artefacts are the small damages that modify
460 pore morphology during drying. Among all of them, Type-II and III are the most spectacular and large enough to
461 modify microstructure significantly. The morphology of the type-II and III drying artefacts are characterized by
462 large irregular shaped very elongated pores with serrated pore boundaries. However, in the present study, the large
463 clay domains and silt-adjacent pores in all samples potentially show smooth edges and rounded pore tip-end, which
464 are incompatible with the typical morphologies of the drying artefacts (Fig.5, 6 and 7). Hence, drying artefacts
465 appear to be less important for reconciling a mismatch between MAD and BIB-SEM porosity.

466 Shallow samples from Unit-I are richer in smectite content than the deeper samples. The moisture and density
467 method (MAD) may overestimate the measured porosity of the sediment if interlayer water from smectite is
468 included in the measurement (Brown and Ransom, 1996; Dutilleul et al., 2020). Greater smectite content in the
469 shallow samples (Unit-I) may have contributed to an overestimation of the MAD porosity in the study.

470 Micromechanical model for porosity reduction

471 Sharp reduction in porosity at the shallow depth from the seafloor to 28 mbsf

472 High porosity (80% MAD; 32% BIB-SEM) in the shallowest sediments is attributed to large pores in the samples
473 created by abundant EE and EF particle contacts (Fig. 5a and 7a). These contacts are unstable and collapse under
474 low effective stress to form FF contacts, resulting in a rapid porosity decrease within the first 28m of burial
475 (Supplementary data-11). This deformation is apparent from the reduction of large clay domain pores observed
476 over this interval (Fig. 8; Supplementary data-10). Collapse of pores surrounded by EE and EF contacts is further
477 recognized by the progressive alignment of clay particles into the bedding plane, which promotes an increase in

478 the number of elongated, small, clay domain pores parallel to the bedding plane. Each of these observations is
479 consistent with rotation of clay particles into the bedding plane as these large clay-domain pores collapse.

480 Mechanism of porosity reduction from 28 mbsf to 1500 mbsf

481 Below 28 mbsf to >1500 mbsf, porosity continues to decrease from 52-30% (MAD) but at a reduced pace. SEM
482 observations suggest that this porosity decline results from the progressive loss of silt-adjacent pores with large
483 silt-adjacent pores lost before small ones (Fig. 8), although they remain present in common abundance to 1200
484 mbsf. Small clay domain pores are abundant throughout the section, and the large clay domain pores are lost
485 above 28 mbsf.

486 Within the population of silt-adjacent pores, the large, equant pores are most susceptible to collapse (Fig. 8). Large,
487 elongate pores persist in abundance, both in linear and crescent geometries. While it seems plausible that large,
488 equant pores collapse to form large, elongate pores, no corresponding increase in the elongate pore population is
489 observed. Large, elongate pores may collapse further and become small silt-adjacent pores. Microstructural
490 evidence supports the idea that large equant pores collapse as surrounding clay particles within clay-rich domains
491 bend and shrink the size of the remaining pore (Fig. 13), and that the collapse results in an increasing aspect ratio
492 of the pore.

493 Frequently, bent clay particles are observed on the top of larger silt-adjacent pores. In the clay microstructure,
494 large silt-adjacent pores act as a zone of heterogeneous strain localization. Clay particles can bend and collapse
495 into large silt-adjacent pores more readily than the smaller pores in the clay matrix (Fig. 13a to f). With increasing
496 vertical effective stress two situations can arise which are demonstrated in the model shown in Fig. 13g. First, with
497 an increase in effective stress, the bent clay particles can lose frictional resistance from the sidewall (Fig. 13a and
498 b), can continue to bend, and slide down to fill the larger silt-adjacent pore space (Fig. 13g-(iii)). Second, with an
499 increase in vertical effective stress, bent clay particles may develop fractures (red lines in Fig. 13g-(iv)) and
500 subsequently collapse into the larger silt-adjacent pore space to reduce the porosity of samples (Fig. 13g-(v)).
501 Fig. 13a represents fractured bent clay on the top of the larger silt adjacent pore (shown by white arrow). Similarly,
502 two small clay particles appear to have fallen into the larger silt adjacent pore space (Fig. 13e) while another bent
503 clay particle (shown by white arrow) covers the pore. Fig. 13f represents a bent clay particle wrapping across the
504 top of two quartz particles, and four small clay platelets fill the space between two quartz particles, suggesting an
505 older, larger silt-adjacent pore filled by fractured clay platelets. Occurring within the pore space between two
506 equant quartz grains (Fig. 13f), four small clay particles appear to have developed due to the fracturing of two large
507 bent clay particles. Hence, it appears that the collapse of larger silt-adjacent pores in these mud samples is governed
508 by the bending of clay particles and subsequent fracturing due to an increase in vertical effective stress. While
509 these processes are defined within individual pores, the observed deformation is interpreted to result from an
510 imposed force chain that acts on specific pores in a progressive manner as the force chain evolves and as adjacent
511 pores deform.

512 Small silt-adjacent pores also become less abundant with burial, but the transition occurs deeper than the large
513 pores, and small, silt-adjacent pores remain common throughout the section (Fig. 8; Supplementary data-11).
514 Small equant pores are lost like the large pores, and elongate pores remain abundant within this population subset

515 throughout. There is a loose correspondence between the loss of small, equant pores and an increase in elongate
516 pores, suggesting that pore flattening is part of the pore collapse history. The pore collapse evolution outlined for
517 large pores (Fig.13g) appears to also hold for small pores, even though observations are more challenging.

518 Small, clay domain pores appear to remain resilient throughout the compaction history (Fig. 8), even though some
519 of these pores must become lost to account for porosity loss. Small, equant pores are lost between 100-200 m, and
520 this loss appears to be accommodated by an increase in elongate pores (Fig. 8). Elongate crescent pores increase
521 in abundance around 800 mbsf, and we interpret this to reflect folding of abundant linear elongate pores as the
522 overall system compacts.

523 Large equant pores in the clay domain are lost within the first few 10's of meters of burial. Elongate pores appear
524 to form at the expense of equant pores, and there may be a reduction in pore size associated with this shape change.
525 Most of the pores remaining after 1500 m of burial are small, elongate pores found both in clay domain and silt-
526 adjacent pores.

527 The presence of silt particles locally redistributes the force chain of load to retain undeformed, silt-adjacent, large
528 pores (Schneider et al., 2011). The samples with greater silt content are also enriched in equant-shaped silt-adjacent
529 larger pores (Fig.10) in the microstructure. Hence, as a result, they display greater porosity compared to other
530 samples from similar depth intervals (Fig.10).

531 Previous studies report contrasting ideas on the development of phyllosilicate fabric strength due to mechanical
532 compaction. Some studies suggest that mechanical compaction creates a phyllosilicate fabric in mud (Bowles et
533 al., 1969; Oertel and Curtis, 1972; Vasseur et al., 1995), whereas other studies conclude that vertical effective
534 stress has limited impact on phyllosilicate fabric development (Ho et al., 1999; Aplin et al., 2006; Day-Stirrat et
535 al., 2008; 2011). Here, we consider the preferred orientation of pores as a proxy for the alignment of phyllosilicate
536 (Hemes et al., 2013). At shallow depth (Unit-I), a weak preferred alignment of the long axis of pores with maxima
537 oriented obliquely to the bedding planes is formed (Supplementary data-15), and at greater depth (Unit-II and III)
538 the long axes of pores become aligned subparallel to the bedding plane. Increase in vertical effective stress below
539 28mbsf depth creates only a small increase in the preferred orientation of the long axis of pores. Hence, we found
540 only a limited change in phyllosilicate fabric strength with increasing vertical stress.

541 Previous authors also document the evolution of pore size distributions in mud with an increase in consolidation
542 stress using laboratory experiments and mercury-intrusion porosimetry (Griffiths and Joshi, 1989; 1990). They
543 conclude that the pore size distribution appears to be bi-modal, and the distribution curve shifts toward smaller
544 pore sizes with an increase in applied consolidation stress (Griffiths and Joshi, 1989). We observe an initial
545 transition from tri-modal to bi-modal pore size distribution around 28mbsf depth due to rapid collapse of large
546 clay domain pores by compactional strain. With an increase in depth below 28mbsf, the bi-modal pore size
547 distribution persists and tends to shift toward small pore sizes as the number of larger silt-adjacent pores
548 diminishes.

549 Laboratory studies have emphasized the importance of clay particle rotation as a dominant mechanism for
550 mechanical compaction in mudstone (Bennett et al., 1981, 1991; Vasseur et al., 1995; Aplin et al., 2006; Day-

551 Stirrat et al., 2008; 2011). We observe particle rotation only in the shallowest samples where unstable EE and EF
552 particle contacts are present. Clay particle bending and sliding/fracturing are considered more important for most
553 of the section studied.

554 Mechanical compaction of marine sediment: a conceptual model

555 According to earlier studies (Delage and Lefebvre, 1984; Griffiths and Joshi, 1989; 1990; Emmanuel and Day-
556 Stirrat 2012), the reduction of pores in sedimentary rocks during compaction is size-dependent - larger pores
557 deform much readily than smaller pores. According to their model, larger pores rapidly decrease in size during
558 compaction to reduce the overall porosity of the sample. However, microstructural analysis of Sumatra samples
559 suggests that porosity reduction is accomplished by compaction of all pore sizes. Moreover, the maximum size of
560 pores remains almost constant irrespective of increasing vertical effective stress/depth (Supplementary data-8)
561 with little difference observed for the maximum pore size in samples from 98.25 mbsf and 1299.31 mbsf. The
562 preservation of a constant ratio between MAD and BIB-SEM porosity measurements (Fig. 3b) suggests that
563 porosity loss is distributed across all pore sizes. We infer that all pore sizes are available for compaction for every
564 increment of applied stress but acknowledge that pore size reduction in different size classes may proceed at
565 different rates.

566 We propose a new model for the reduction in porosity in which all pores within the force chain of load take part
567 in the reduction of porosity during compaction irrespective of their size. At shallow depth up to 28mbsf, larger
568 clay-domain pores are the most susceptible to early response during an increase in compactional strain, because of
569 two reasons: 1) the 'domains' defined by the clay particles are weaker compared to the larger, rigid silt grains, and
570 2) due to higher relative proportion of clay-rich regions within the mud, the force chain of load dominantly passes
571 through the clay domains. The dispersed nature of the silt-size particles and the high proportion of phyllosilicates
572 in the mud samples indicate that soft clay particles act as the principal load-bearing framework. Hence, larger clay
573 domain pores are more unstable compared to silt-adjacent pores in the mud microstructure. Similarly, below
574 28mbsf depth, under an increase in vertical effective stress, both the larger silt-adjacent pores and smaller pores in
575 the clay matrix that come within the force chain of load collapse. Hence, the ratio between BIB-SEM porosity vs
576 MAD porosity remains almost constant irrespective of the depth. All larger silt-adjacent pores do not come within
577 the force chain of load at the same time. Hence, some of the larger silt-adjacent pores remained undeformed to the
578 maximum depth of 1500mbsf depth. Therefore, the maximum size of the larger silt-adjacent pores remains almost
579 constant irrespective of the depth/vertical effective stress.

580 While our understanding of how different pore types is consistent with all available data, tracking the pore
581 evolution through additional size categories would elucidate the pore evolution in more detail. Preliminary pore
582 size distribution data (Fig.9) indicate that 4 size bins exist in these samples. Developing this approach requires
583 improved image analysis techniques to tie all the pore attributes together on a pore-by-pore basis for a huge number
584 of pores.

585 Compaction strain accommodation and grain-scale deformation

586 Deformation of clay-rich sedimentary rocks involves four possible mechanisms: 1) Particulate flow; (Morgenstern
587 and Tchalenko, 1967; Borradaile et al., 1981); 2) Cataclasis; (Ukar and Cloos, 2019) 3) Diffusive mass transfer;
588 (Blenkinsop, 2007; Fossen, 2016); 4) Intercrystalline plasticity (Blenkinsop, 2007; Fossen, 2016). Intensity and
589 occurrence of a particular deformation mechanism in a mudstone depend on several parameters, such as effective
590 stress, water content, cementation, temperature (Desbois et al., 2017; Den Hartog and Spiers, 2014).

591 All our samples show evidence of particulate flow controlled by friction between grains. At shallow depths, illite
592 platelets contacted at EE and EF junctions lose these weak bonds, and particles rotate into bedding-parallel
593 orientation. Once FF contacts dominate, large-scale rotations are reduced, and **intra-particle slip** becomes
594 important. This is best evidenced in collapse of large, silt-adjacent pores where bent clay particles overlie pores
595 (Fig. 14a to f). In deforming granular foam material, bending was reported as the dominant deformation mechanism
596 for the reduction in porosity and developing preferred alignment of the long axis of pores perpendicular to the
597 applied stress (Elliott et al., 2002, Zhou et al., 2004; Samsudin et al., 2017; Zakaria et al., 2018) (review of these
598 **earlier studies on the experimental deformation of granular foam is described in document S2**). Friction adheres
599 clay particles to the edge of pores while the middle of particles drops into the pore, resulting in bending by **intra-**
600 **particle slip**. A cartoon (Fig. 14g) illustrates the compaction mechanism associated with the bending of clay
601 particles. With increasing compaction strain, clay particles undergo bending, and as a result, pore area reduces,
602 and the orientation of the pores tends to align perpendicular to the applied effective stress (Fig. 14g). **At shallow**
603 **depths (Unit-I), particles get enough free space for rotation to align parallel to the bedding plane because of higher**
604 **porosity (Figure S12a and b). However, at greater depth where porosity decreases, space problems limit particle**
605 **deformation to bending and fracturing as increase in compactional strain increases (Figure S12c and d).**

606 Compaction of Sumatra input section: generalized implication for rock property 607 evolution

608 The overall compaction curve obtained for Sumatra muds is comparable with the experimental study by Fawad et
609 al., 2010 in the context of compactional range (Fig.8). The curve shows a mono-exponential decrease in porosity
610 with an increase in vertical effective stress, which is evidence of normal consolidation (Fawad et al., 2010;
611 Dutilleul et al., 2020).

612 The larger silt-adjacent pores seen in the deepest of these samples (1500 m burial) suggest these muds retain
613 considerable potential for additional **mechanical** compaction with deeper burial. As this marine sediment
614 progressively approaches greater burial closer **to** the accretionary prism, it will undergo further change in physical
615 and deformational properties (Bray and Karig, 1985). Despite the substantial compactional strain, the relatively
616 high porosity of the deepest sample and the survival of larger and mechanically unstable silt-margin pores suggests
617 that compactional stabilization has yet to be reached because such IGVs and pore types are not generally observed
618 in older and lithified mudrocks. Based on the current understanding of subduction zone deformation behavior and
619 mudrock properties, it seems likely that **mechanical** compaction will continue to dominate the pore loss in deeper
620 burial.

621 The general absence of early cementation and the corresponding dominance of compaction in the total pore loss is
622 consistent with observations of other siliciclastic-dominated muds (Milliken, 2014; 2019). The trends for
623 intergranular volume change observed from the seafloor and 1500mbsf place useful constraints on the maximum
624 cement volumes that theoretically could be emplaced at this depth range in sediments containing a more reactive
625 grain assemblage. At the depths of burial attained at the deformation front, any cementation of the Sumatra input
626 sediments will be limited to <30% of the rock volume, or possibly much less, as mechanical compaction is
627 expected to continue up to the burial temperatures that initiate grain reactions and associated cementation.

628 Conclusions

629 Pores are classified by size and microstructural position, resulting in a multi-modal contribution to the total
630 porosity. Shallow samples (seafloor to 28 mbsf) display a sharp reduction in porosity from 80% to 52% as large
631 clay domain/matrix pores collapse. Deeper samples (28 mbsf to 1500 mbsf) exhibit a smaller reduction in porosity
632 from 50% to 32% due to the collapse of silt-adjacent pores by bending and subsequent fracturing/sliding of clay
633 particles.

634 The class of large pores next to silt-sized grains (between 10^4 and 10^6 nm²) remains common to >1 km burial,
635 irrespective of the mineralogy of the silt-sized grains, but their size decreases with depth. Small, equant pores next
636 to silt particles are abundant in the first 100 m of burial and remain common over the entire depth range.

637 Small pores in clay domains are almost all elongated, and abundant over all observed depths. Small, crescent-
638 shaped elongate pores increase in abundance with depth as clay particles become folded by compactional
639 processes.

640 The size-independence of pore loss arises because the force chain driving pore collapse is localized primarily
641 within the volumetrically dominant and weaker clay-rich domains; larger pores around isolated silt particles enter
642 into the force chain somewhat randomly and asynchronously and do not contribute preferentially to pore loss over
643 the depth range studied.

644 An increase in effective stress up to 18MPa (~1500 mbsf) causes the development of weakly aligned phyllosilicate
645 fabric (defined by mica and illite clay particles) in the microstructure.

646 Compaction processes in our samples are dominated by granular flow (rotation and frictional sliding of illite clay
647 particles) at shallow depths. With increasing depth, compaction is additionally accommodated by bending of clay
648 particles.

649 Data availability

650 High resolution SE2 and BSE images of all samples are available online at:

651 <https://figshare.com/s/cbaada517b0b1409d575>

652 Authors contributions

653 SL and KLM performed sample preparation and BIB-SEM microscopy. SL analysed the data. JLU and GD
654 acquired funding. JLU managed the project. PV, KLM and JLU significantly contributed to interpret the data. SL
655 wrote the first draft of the manuscript. PV, KLM and JLU contributed for the correction and improvement of the
656 manuscript.

657 Competing interests

658 The authors declare that they do not have any conflict of interest.

659 Acknowledgments

660 SL and JLU thank German Research Foundation (Deutsche Forschungsgemeinschaft [DFG] grant UR 64/19-1)
661 for providing funding to carry out the research. IODP (International Ocean Discovery Programme) sample
662 repository, Japan is acknowledged for providing oriented mud samples for the study. KLM acknowledges the
663 samples and data provided by the International Ocean Discovery Program (IODP). Funding for sample preparation
664 and SEM imaging was supported by a post-expedition award (Milliken, P.I.) from the Consortium for Ocean
665 Leadership. SL thanks Manuel Menzel, Jop Klaver, Liene Spruženiece, and Joyce Schmatz for providing valuable
666 time to teach BIB-SEM techniques. We would like to thank Dave Duehurst and Bernhard Schuck for their
667 constructive ideas in the review reports, and Virginia Toy for editorial handling.

668 References

- 669 Adams, R. and Bischof, L.: Seeded region growing. IEEE Transactions on pattern analysis and machine
670 intelligence. IEEE: 16(6), 641-647. [https://DOI. 10.1109/34.295913](https://doi.org/10.1109/34.295913), 1994.
- 671 Ajdukiewicz, J. M. and Lander, R. H.: Sandstone reservoir quality prediction: state of the art, AAPG Bulletin, 94,;
672 1082-1091, [https:// doi.org/10.1306/intro060110](https://doi.org/10.1306/intro060110), 2010.
- 673 Ammon, C.J., Ji, C., Thio, H.K., Robinson, D., Ni, S., Hjorleifsdottir, V., Kanamori, H., Lay, T., Das, S.,
674 Helmberger, D. and Ichinose, G. Rupture process of the 2004 Sumatra-Andaman earthquake, Science, 308(5725),
675 1133-1139, DOI: 10.1126/science.1112260, 2005.
- 676 Aplin, A.C. and Macquaker, J.H.: Mudstone diversity: Origin and implications for source, seal, and reservoir
677 properties in petroleum systems, AAPG bulletin, 95(12), 2031-2059, <https://doi.org/10.1306/03281110162>, 2011.
- 678 Aplin, A.C., Matenaar, I.F. and Vvan Dder Pluijm, B.A.: Influence of mechanical compaction and chemical
679 diagenesis on the microfabric and fluid flow properties of Gulf of Mexico mudstones Journal of Geochemical
680 Exploration, 78, 449-451, [https://doi.org/10.1016/S0375-6742\(03\)00035-9](https://doi.org/10.1016/S0375-6742(03)00035-9), 2003.

681 Aplin, A.C., Matenaar, I.F., McCarty, D.K. and Vvan Der Pluijm, B.A.: Influence of mechanical compaction and
682 clay mineral diagenesis on the microfabric and pore-scale properties of deep-water Gulf of Mexico mudstones,
683 *Clays and Clay Minerals*, 54(4), 500-514, <https://doi.org/10.1346/CCMN.2006.0540411>, 2006.

684 Backman, J., Chen, W., Kachovich, S., Mitchison, F. L., Petronotis, K. E., Yang, T. and Zhao, X.: Data report:
685 Revised age models for IODP Sites U1480 and U1481, Expedition 362, Proceedings of the International Ocean
686 Discovery Program, Expedition Reports 362, <https://doi.org/10.14379/iodp.proc.362.202.2019>, 2019.

687 Baruch, E.T., Kennedy, M.J., Löhr, S.C. and Dewhurst, D.N.: Feldspar dissolution-enhanced porosity in
688 Paleoproterozoic shale reservoir facies from the Barney Creek Formation (McArthur Basin, Australia). *AAPG*
689 *Bulletin*, 99(9), 1745-1770, <https://doi.org/10.1306/04061514181>, 2015.

690 Bennett, R.H., Bryant, W.R. and Keller, G.H.: Clay fabric of selected submarine sediments; fundamental properties
691 and models, *Journal of Sedimentary Research*, 51(1), 217-232, [https://doi.org/10.1306/212F7C52-2B24-11D7-](https://doi.org/10.1306/212F7C52-2B24-11D7-8648000102C1865D)
692 [8648000102C1865D](https://doi.org/10.1306/212F7C52-2B24-11D7-8648000102C1865D), 1981.

693 Bennett, R.H., O'Brien, N.R. and Hulbert, M.H.: Determinants of clay and shale microfabric signatures: processes
694 and mechanisms. In *Microstructure of Fine-Grained Sediments*, 5-32, Springer, New York, NY. [https://DOI:](https://DOI:10.1007/978-1-4612-4428-8_2)
695 [10.1007/978-1-4612-4428-8_2](https://DOI:10.1007/978-1-4612-4428-8_2), 1991.

696 Blenkinsop, T.G.: *Deformation microstructures and mechanisms in minerals and rocks*, Springer Science &
697 Business Media, 2007.

698 Bowles, F.A., Bryant, W.R. and Wallin, C.: Microstructure of unconsolidated and consolidated marine sediments,
699 *Journal of Sedimentary Research*, 39(4), 1546-1551, [https://doi.org/10.1306/74D71E7E-2B21-11D7-](https://doi.org/10.1306/74D71E7E-2B21-11D7-8648000102C1865D)
700 [8648000102C1865D](https://doi.org/10.1306/74D71E7E-2B21-11D7-8648000102C1865D), 1969.

701 Borradaile, G.J.: Particulate flow of rock and the formation of cleavage. *Tectonophysics*, 72(3-4), 305-321,
702 [https://doi.org/10.1016/0040-1951\(81\)90243-2](https://doi.org/10.1016/0040-1951(81)90243-2), 1981.

703 Bray, C.J. and Karig, D.E.: Porosity of sediments in accretionary prisms and some implications for dewatering
704 processes, *Journal of Geophysical Research: Solid Earth*, 90(B1), 768-778, [https://doi.org/](https://doi.org/10.1029/JB090iB01p00768)
705 [10.1029/JB090iB01p00768](https://doi.org/10.1029/JB090iB01p00768), 1985.

706 Brown, K.M. and Ransom, B.: Porosity corrections for smectite-rich sediments: Impact on studies of compaction,
707 fluid generation, and tectonic history. *Geology*, 24(9), 843-846, [https://doi.org/10.1130/0091-](https://doi.org/10.1130/0091-7613(1996)024<0843:PCFSRS>2.3.CO;2)
708 [7613\(1996\)024<0843:PCFSRS>2.3.CO;2](https://doi.org/10.1130/0091-7613(1996)024<0843:PCFSRS>2.3.CO;2), 1996.

709 Burland, J.B.: On the compressibility and shear strength of natural clays. *Géotechnique*, 40(3), 329-378,
710 doi.org/10.1680/geot.1990.40.3.329, 1990.

711 Chester, F.M., Rowe, C., Ujiie, K., Kirkpatrick, J., Regalla, C., Remitti, F., Moore, J.C., Toy, V., Wolfson-
712 Schwehr, M., Bose, S. and Kameda, J.: Structure and composition of the plate-boundary slip zone for the 2011
713 Tohoku-Oki earthquake. *Science*, 342(6163), 1208-1211, [https://DOI: 10.1126/science.1243719](https://doi.org/10.1126/science.1243719), 2013.

714 Day-Stirrat, R.J., Aplin, A.C., Środoń, J. and Van der Pluijm, B.A.: Diagenetic reorientation of phyllosilicate
715 minerals in Paleogene mudstones of the Podhale Basin, southern Poland, *Clays and Clay Minerals*, 56(1), 100-
716 111, DOI: 10.1346/CCMN.2008.0560109, 2008.

717 Day-Stirrat, R.J., Flemings, P.B., You, Y., Aplin, A.C. and van der Pluijm, B.A.: The fabric of consolidation in
718 Gulf of Mexico mudstones, *Marine Geology*, 295, 77-85, <https://doi.org/10.1016/j.margeo.2011.12.003>, 2012.

719 Day-Stirrat, R.J., Milliken, K.L., Dutton, S.P., Loucks, R.G., Hillier, S., Aplin, A.C. and Schleicher, A.M.: Open-
720 system chemical behavior in deep Wilcox Group mudstones, Texas Gulf Coast, USA, *Marine and Petroleum*
721 *Geology*, 27(9), 1804-1818, <https://doi.org/10.1016/j.marpetgeo.2010.08.006>, 2010.

722 Day-Stirrat, R.J., Schleicher, A.M., Schneider, J., Flemings, P.B., Germaine, J.T. and van der Pluijm, B.A.:
723 Preferred orientation of phyllosilicates: Effects of composition and stress on resedimented mudstone
724 microfabrics, *Journal of Structural Geology*, 33(9), 1347-1358, [https://DOI:10.1016/j.jsg.2011.06.007](https://doi.org/10.1016/j.jsg.2011.06.007), 2011.

725 Dean, S.M., McNeill, L.C., Henstock, T.J., Bull, J.M., Gulick, S.P., Austin, J.A., Bangs, N.L., Djajadihardja, Y.S.
726 and Permana, H.: Contrasting décollement and prism properties over the Sumatra 2004–2005 earthquake rupture
727 boundary, *Science*, 329(5988), 207-210, [https://DOI: 10.1126/science.1189373](https://doi.org/10.1126/science.1189373), 2010.

728 Delage, P. and Lefebvre, G.: Study of the structure of a sensitive Champlain clay and of its evolution during
729 consolidation. *Canadian Geotechnical Journal*, 21(1), 21-35, <https://doi.org/10.1139/t84-003>, 1984.

730 Delle Piane, C., Almqvist, B.S., MacRae, C.M., Torpy, A., Mory, A.J. and Dewhurst, D.N.: Texture and diagenesis
731 of Ordovician shale from the Canning Basin, Western Australia: Implications for elastic anisotropy and
732 geomechanical properties. *Marine and Petroleum Geology*, 59, 56-71, doi.org/10.1016/j.marpetgeo.2014.07.017,
733 2015.

734 Den Hartog, S. A. and Spiers, C. J.: A microphysical model for fault gouge friction applied to subduction
735 megathrusts, *Journal of Geophysical Research: Solid Earth*, 119(2), 1510-1529.
736 <https://doi.org/10.1002/2013JB010580>, 2014.

737 Desbois, G., Urai, J.L. and Kukla, P.A.: Morphology of the pore space in claystones—evidence from BIB/FIB ion
738 beam sectioning and cryo-SEM observations. *eEarth Discussions*, 4(1), 1-19, 2009.

739 Desbois, G., Urai, J.L., Hemes, S., Brassinnes, S., De Craen, M. and Sillen, X.: Nanometer-scale pore fluid
740 distribution and drying damage in preserved clay cores from Belgian clay formations inferred by BIB-cryo-
741 SEM. *Engineering Geology*, 179, 117-131, <https://doi.org/10.1016/j.enggeo.2014.07.004>, 2014.

742 Desbois, G., Höhne, N., Urai, J. L., Bésuelle, P., and Viggiani, G.: Deformation in cemented mudrock (Callovo–
743 Oxfordian Clay) by microcracking, granular flow and phyllosilicate plasticity: insights from triaxial deformation,
744 broad ion beam polishing and scanning electron microscopy, *Solid Earth*, 8, 291–305, [https://doi.org/10.5194/se-](https://doi.org/10.5194/se-8-291-2017)
745 8-291-2017, 2017.

746 Desbois, G., Urai, J. L., Kukla, P. A., Konstanty, J., & Baerle, C.: High-resolution 3D fabric and porosity model
747 in a tight gas sandstone reservoir: A new approach to investigate microstructures from mm-to nm-scale combining
748 argon beam cross-sectioning and SEM imaging. *Journal of Petroleum Science and Engineering*, 78(2), 243-257,
749 <https://doi.org/10.1016/j.petrol.2011.06.004>, 2011.

750 Dugan, B., McNeill, L. and Petronotis, K.: Expedition 362 preliminary report: Sumatra subduction zone,
751 International Ocean Discovery Program, 2017.

752 Dutilleul, J., Bourlange, S., Conin, M. and Géraud, Y.: Quantification of bound water content, interstitial porosity
753 and fracture porosity in the sediments entering the North Sumatra subduction zone from Cation Exchange Capacity
754 and IODP Expedition 362 resistivity data, *Marine and Petroleum Geology*, 111, 156-165.,
755 <https://doi.org/10.1016/j.marpetgeo.2019.08.007>, 2020.

756 Ehrenberg, S. N.: Assessing the relative importance of compaction processes and cementation to reduction of
757 porosity in sandstones: discussion. *American Association of Petroleum Geologists Bulletin*, 73, 1274-1276,
758 <https://doi.org/10.1306/44B4AA1E-170A-11D7-8645000102C1865D>, 1989.

759 Elliott, J.A., Windle, A.H., Hobdell, J.R., Eeckhaut, G., Oldman, R.J., Ludwig, W., Boller, E., Cloetens, P. and
760 Baruchel, J.: In-situ deformation of an open-cell flexible polyurethane foam characterised by 3D computed
761 microtomography, *Journal of materials science*, 37(8), 1547-1555, doi:10.1023/A:1014920902712, 2002.

762 Emmanuel, S. and Day-Stirrat, R.J.: 2012. A framework for quantifying size dependent deformation of nano-scale
763 pores in mudrocks *Journal of applied geophysics*, 86, 29-35, <https://doi.org/10.1016/j.jappgeo.2012.07.011>, 2012.

764 Fawad, M., Mondol, N.H., Jahren, J. and Bjørlykke, K.: Microfabric and rock properties of experimentally
765 compressed silt-clay mixtures, *Marine and Petroleum Geology*, 27(8), 1698-1712,
766 <https://doi.org/10.1016/j.marpetgeo.2009.10.002>, 2010.

767 Fossen, H.: *Structural geology*. Cambridge university press. 2016.

768 Ghosal, D., Singh, S.C. and Martin, J.: Shallow subsurface morphotectonics of the NW Sumatra subduction system
769 using an integrated seismic imaging technique, *Geophysical Journal International*, 198(3), 1818-1831,
770 <https://doi.org/10.1093/gji/ggu182>, 2014.

771 Griffiths, F.J. and Joshi, R.C.: Change in pore size distribution due to consolidation of clays. *Geotechnique*, 39(1),
772 159-167, doi.org/10.1680/geot.1989.39.1.159, 1989.

773 Griffiths, F.J. and Joshi, R.C.: Clay fabric response to consolidation. *Applied clay science*, 5(1), 37-66,
774 doi.org/10.1016/0169-1317(90)90005-A, 1990.

775 Griffiths, F.J. and Joshi, R.C.: Change in pore size distribution owing to secondary consolidation of
776 clays. *Canadian Geotechnical Journal*, 28(1), 20-24, <https://doi.org/10.1139/t91-003>, 1991.

777 Hemes, S., Desbois, G., Klaver, J. and Urai, J.L.: Microstructural characterisation of the Ypresian clays (Kallo-1)
778 at nanometre resolution, using broad-ion beam milling and scanning electron microscopy. *Netherlands Journal of*
779 *Geosciences*, 95(3), 293-313, DOI: <https://doi.org/10.1017/njg.2016.16>, 2016.

780 Hemes, S., Desbois, G., Urai, J.L., De Craen, M. and Honty, M.: Variations in the morphology of porosity in the
781 Boom Clay Formation: insights from 2D high resolution BIB-SEM imaging and Mercury injection
782 Porosimetry. *Netherlands Journal of geosciences*, 92(4), 275-300, DOI: doi.org/10.1017/S0016774600000214,
783 2013.

784 Hemes, S., Desbois, G., Urai, J.L., Schröppel, B. and Schwarz, J.O.: Multi-scale characterization of porosity in
785 Boom Clay (HADES-level, Mol, Belgium) using a combination of X-ray μ -CT, 2D BIB-SEM and FIB-SEM
786 tomography. *Microporous and mesoporous materials*, 208, 1-20, [https://](https://doi.org/10.1016/j.micromeso.2015.01.022)
787 doi.org/10.1016/j.micromeso.2015.01.022, 2015.

788 Hesse, R.: Turbiditic and non-turbiditic mudstone of Cretaceous flysch sections of the East Alps and other
789 basins. *Sedimentology*, 22(3), 387-416, <https://doi.org/10.1111/j.1365-3091.1975.tb01638.x>, 1975.

790 Hippchen, S. and Hyndman, R.D.: Thermal and structural models of the Sumatra subduction zone: Implications
791 for the megathrust seismogenic zone. *Journal of Geophysical Research: Solid Earth*, 113(B12), [https://doi.org/10.](https://doi.org/10.1002/2015TC003901)
792 <https://doi.org/10.1002/2015TC003901>, 2008.

793 Ho, N.C., Peacor, D.R. and Van der Pluijm, B.A.: Preferred orientation of phyllosilicates in Gulf Coast mudstones
794 and relation to the smectite-illite transition. *Clays and Clay Minerals*, 47(4), 495-504, DOI: 10.1346/CCMN.
795 1999.0470412, 1999.

796 Houben, M.E., Desbois, G. and Urai, J.L.: A comparative study of representative 2D microstructures in Shaly and
797 Sandy facies of Opalinus Clay (Mont Terri, Switzerland) inferred from BIB-SEM and MIP methods, *Marine and*
798 *Petroleum Geology*, 49, 143-161, <https://doi.org/10.1016/j.marpetgeo.2013.10.009>, 2014.

799 Hüpers, A., Ikari, M.J., Dugan, B., Underwood, M.B. and Kopf, A.J.: Origin of a zone of anomalously high
800 porosity in the subduction inputs to Nankai Trough. *Marine Geology*, 361, 147-162,
801 <https://doi.org/10.1016/j.margeo.2015.01.004>, 2015.

802 Hüpers, A., Torres, M.E., Owari, S., McNeill, L.C., Dugan, B., Henstock, T.J., Milliken, K.L., Petronotis, K.E.,
803 Backman, J., Bourlange, S. and Chemale, F.: Release of mineral-bound water prior to subduction tied to shallow
804 seismogenic slip off Sumatra. *Science*, 356(6340), 841-844. 2017.

805 Jiang, M., Klaver, J., Schmatz, J. and Urai, J.L.: Nanoscale porosity analysis in geological materials. *Acta*
806 *Stereologica*, 2015.

807 Kameda, A., Dvorkin, J., Keehm, Y., Nur, A. and Bosl, W.: Permeability-porosity transforms from small sandstone
808 fragments. *Geophysics*, 71(1), N11-N19, <https://doi.org/10.1190/1.2159054>, 2006.

809 Karaborni, S., Smit, B., Heidug, W., Urai, J. and Van Oort, E.: The swelling of clays: molecular simulations of
810 the hydration of montmorillonite. *Science*, 271(5252), 1102-1104, DOI: 10.1126/science.271.5252.1102, 1996.

811 Klaver, J., Desbois, G., Littke, R. and Urai, J.L.: BIB-SEM characterization of pore space morphology and
812 distribution in postmature to overmature samples from the Haynesville and Bossier Shales. *Marine and petroleum*
813 *Geology*, 59, 451-466, <https://doi.org/10.1016/j.marpetgeo.2014.09.020>, 2015.

814 Klaver, J., Desbois, G., Littke, R. and Urai, J.L.: BIB-SEM pore characterization of mature and post mature
815 Posidonia Shale samples from the Hils area, Germany. *International Journal of Coal Geology*, 158, 78-89,
816 <https://doi.org/10.1016/j.coal.2016.03.003>, 2016.

817 Klaver, J., Desbois, G., Urai, J.L. and Littke, R.: BIB-SEM study of the pore space morphology in early mature
818 Posidonia Shale from the Hils area, Germany. *International Journal of Coal Geology*, 103, 12-25.
819 <https://doi.org/10.1016/j.coal.2012.06.012>, 2012.

820 Kuila, U. and Prasad, M.: Specific surface area and pore-size distribution in clays and shales. *Geophysical*
821 *Prospecting*, 61(2-Rock Physics for Reservoir Exploration, Characterisation and Monitoring), pp.341-362,
822 <https://doi.org/10.1111/1365-2478.12028>, 2013.

823 Lander, R. H. and Walderhaug, O. W.: Predicting porosity through simulating sandstone compaction and quartz
824 cementation. *American Association of Petroleum Geologists Bulletin* 83: 433-449,
825 <https://doi.org/10.1306/00AA9BC4-1730-11D7-8645000102C1865D>, 1999.

826 Lander, R. H., Larese, R. H. Larese and Bonnell, L. M.: Toward more accurate quartz cement models: The
827 importance of euhedral versus noneuhedral growth rates. *American Association Petroleum Geologists Bulletin* 92:
828 1537-1563. <https://doi.org/10.1306/07160808037>, 2008.

829 Laurich, B., Urai, J.L., Desbois, G., Vollmer, C. and Nussbaum, C.: Microstructural evolution of an incipient fault
830 zone in Opalinus Clay: Insights from an optical and electron microscopic study of ion-beam polished samples from
831 the Main Fault in the Mt-Terri Underground Research Laboratory. *Journal of Structural Geology*, 67, 107-128.
832 <https://doi.org/10.1016/j.jsg.2014.07.014>, 2014.

833 Lay, T., Kanamori, H., Ammon, C. J., Nettles, M., Ward, S.N., Aster, R.C., Beck, S.L., Bilek, S.L., Brudzinski,
834 M.R., Butler, R. and DeShon, H.R.: The great Sumatra-Andaman earthquake of 26 Ddecember
835 2004. *Sscience*, 308(5725), pp.1127-1133, DOI: 10.1126/science.1112250, 2005.

836 Lazar, O.R., Bohacs, K.M., Macquaker, J.H., Schieber, J. and Demko, T.M.: Capturing key attributes of fine-
837 grained sedimentary rocks in outcrops, cores, and thin sections: nomenclature and description guidelines. *Journal*
838 *of Sedimentary Research*, 85(3), pp.230-246, <https://doi.org/10.2110/jsr.2015.11>, 2015.

839 Lundegard, P. D.: Sandstone porosity loss--a 'big picture' view of the importance of compaction. *Journal of*
840 *Sedimentary Petrology* 62: 250-260, <https://doi.org/10.1306/D42678D4-2B26-11D7-8648000102C1865D>, 1992.

841 McNeill, L.C., Dugan, B. and Petronotis, K.E., Backman, J., Bourlange, S., Chemale, F., Chen, W., Colson, T.A.,
842 Frederik, M.C.G., Guèrin, G., Hamahashi, M., Henstock, T., House, B.M., Hüpers, A., Jeppson, T.N., Kachovich,
843 S., Kenigsberg, A.R., Kuranaga, M., Kutterolf, S., Milliken, K.L., Mitchison, F.L., Mukoyoshi, H., Nair, N.,
844 Owari, S., Pickering, K.T., Pouderoux, H.F.A., Yehua, S., Song, I., Torres, M.E., Vannucchi, P., Vrolijk, P.J.,
845 Yang, T., and Zhao, X.: Sumatra Subduction Zone. *Proceedings of the International Ocean Discovery*
846 *Program*, 362, <https://doi.org/10.14379/iodp.proc.362.102.2017>, 2017.

847 Meade, R.H.: Removal of water and rearrangement of particles during the compaction of clayey sediments. US
848 Government Printing Office, 1964.

849 Mesri, G. and Olson, R.E.: Mechanisms controlling the permeability of clays. *Clays and Clay minerals*, 19(3),
850 151-158, 1971.

851 Milliken, K. L.: A compositional classification for grain assemblages in fine-grained sediments and sedimentary
852 rocks. *Journal of Sedimentary Research* 84: 1185-1199, <https://doi.org/10.2110/jsr.2014.92>, 2008.

853 Milliken, K. L.: A compositional classification for grain assemblages in fine-grained sediments and sedimentary
854 rocks. *Journal of Sedimentary Research* 84: 1185-1199, <https://doi.org/10.2110/jsr.2014.92>, 2014.

855 Milliken K. L.: Compactional and mass-balance constraints inferred from the volume of quartz cementation in
856 mudrocks. *Mudstone Diagenesis: New Research Perspectives for Shale Hydrocarbon Reservoirs, Seals, and*
857 *Source Rocks*. AAPG. 120: 33-48, DOI: 10.1306/13672209M121252, 2019.

858 Milliken, K. L. and Curtis, M. E.: Imaging pores in sedimentary rocks: Foundation of porosity prediction. *Marine*
859 *and Petroleum Geology* 73,: 590-608, <https://doi.org/10.1016/j.marpetgeo.2016.03.020>, 2016.

860 Milliken, K. L. and Day-Stirrat R. J.: Cementation in mudrocks: Brief review with examples from cratonic basin
861 mudrocks. *Memoir. J.-Y. Chatellier*. Tulsa, Oklahoma, USA, AAPG, <https://doi.org/10.1306/13401729H55252>,
862 2013.

863 Milliken, K. L. and Olson, T.: Silica diagenesis, porosity evolution, and mechanical behavior in siliceous
864 mudstones, Mowry Shale Cretaceous, Rocky Mountains, U.S.A. *Journal of Sedimentary Research* 87: 366-387,
865 <https://doi.org/10.2110/jsr.2017.24>, 2017.

866 Milliken, K. L., Rudnicki, M., Awwiller, D. N. and Zhang, T.: Organic matter-hosted pore system, Marcellus
867 Formation Devonian, Pennsylvania, USA. AAPG Bulletin 97: 177-200, <https://doi.org/10.1306/07231212048>,
868 2013.

869 Milliken, K. L., Esch, W. L., Reed, R. M. and Zhang, T.: Grain assemblages and strong diagenetic overprinting
870 in siliceous mudrocks, Barnett Shale Mississippian, Fort Worth Basin, Texas, U.S.A. AAPG Bulletin 96: 1553-
871 1578, <https://doi.org/10.1306/12011111129>, 2012.

872 Mitchell, J.K.: The fabric of natural clays and its relation to engineering properties. In Highway Research Board
873 Proceedings, 35, 1956.

874 Moeremans, R.E. and Singh, S.C.: Fore-arc basin deformation in the Andaman-Nicobar segment of the Sumatra-
875 Andaman subduction zone: Insight from high-resolution seismic reflection data, Tectonics, 34(8), 1736-1750,
876 doi.org/10.1002/2015TC003901, 2015.

877 Mondol, N.H., Bjørlykke, K., Jahren, J. and Høeg, K.: Experimental mechanical compaction of clay mineral
878 aggregates—Changes in physical properties of mudstones during burial. Marine and petroleum geology, 24(5),
879 289-311, <https://doi.org/10.1016/j.marpetgeo.2007.03.006>, 2007.

880 Morgenstern, N.R. and Tchalenko, J.S.: Microstructural observations on shear zones from slips in natural clays,
881 1967.

882 Nakano, R.: On weathering and change of properties of tertiary mudstone related to landslide. Soils and
883 Foundations, 7(1), 1-14, <https://doi.org/10.3208/sandf1960.7.1>, 1967.

884 Neagu, R.C., Cartwright, J. and Davies, R.: Measurement of diagenetic compaction strain from quantitative
885 analysis of fault plane dip. Journal of Structural Geology, 32(5), 641-655,
886 <https://doi.org/10.1016/j.jsg.2010.03.010>, 2010.

887 Nole, M., Daigle, H., Milliken, K.L. and Prodanović, M.: A method for estimating microporosity of fine-grained
888 sediments and sedimentary rocks via scanning electron microscope image analysis. Sedimentology, 63(6), 1507-
889 1521, <https://doi.org/10.1111/sed.12271>, 2016.

890 Nollet, S., Hilgers, C. and Urai, J.: Sealing of fluid pathways in overpressure cells: a case study from the
891 Buntsandstein in the Lower Saxony Basin (NW Germany). International Journal of Earth Sciences, 94(5), 1039-
892 1055, <https://doi.org/10.1007/s00531-005-0492-1>, 2005.

893 Oelker, A.: Deformation properties of Boom Clay: Implementation of a multi-scale concept. Dissertation,
894 Rheinisch-Westfälische Technische Hochschule Aachen, DOI: 10.18154/RWTH-2019-09913, 2019.

895 Oertel, G. and Curtis, C.D.: Clay-ironstone concretion preserving fabrics due to progressive
896 compaction. Geological Society of America Bulletin, 83(9), 2597-2606, [https://doi.org/10.1130/0016-7606\(1972\)83\[2597:CCPFDT\]2.0.CO;2](https://doi.org/10.1130/0016-7606(1972)83[2597:CCPFDT]2.0.CO;2), 1972.

898 Paxton, S. T., J. O. Szabo, J. M. Adjukiewicz and R. E. Klimentidis.: Construction of an intergranular volume
899 compaction curve for evaluating and predicting compaction and porosity loss in rigid-grain sandstone reservoirs.
900 American Association of Petroleum Geologists Bulletin 86: 2047-2067, [https://doi.org/10.1306/61EEDDFA-](https://doi.org/10.1306/61EEDDFA-173E-11D7-8645000102C1865D)
901 173E-11D7-8645000102C1865D, 2002.

902 Pickering, K.T., Carter, A., Andò, S., Garzanti, E., Limonta, M., Vezzoli, G. and Milliken, K.L.: 2020. Deciphering
903 relationships between the Nicobar and Bengal submarine fans, Indian Ocean. *Earth and Planetary Science*
904 *Letters*, 544, 116329, <https://doi.org/10.1016/j.epsl.2020.116329>, 2020.

905 Pommer, M. E. and Milliken, K. L.: Pore types and pore-size distributions across thermal maturity, Eagle Ford
906 Formation, South Texas. *AAPG Bulletin* 99: 1713-1744, <https://doi.org/10.1306/03051514151>, 2015.

907 Prawirodirdjo, L., Boel, Y., McCaffrey, R., Genrich, J., Calais, E., Stevens, C., Puntodewo, S.S.O., Subarya, C.,
908 Rais, J., Zwick, P. and Fauzi, R.M.: Geodetic observations of interseismic strain segmentation at the Sumatra
909 subduction zone. *Geophysical research letters*, 24(21), 2601-2604, <https://doi.org/10.1029/97GL52691>, 1997.

910 Rieke, H.H. and Chilingarian, G.V.: *Compaction of argillaceous sediments*. Elsevier, 1974.

911 Rosenberger, K., Underwood, M.B., Vrolijk, P. and Haines, S.: Data report: clay mineral assemblages in
912 hemipelagic sediments entering the Sumatra subduction zone, IODP Sites U1480 and U1481, Expedition
913 362. *Expedition*, 362, 1. 2020.

914 Samsudin, M.S.F., Ariff, Z.M. and Ariffin, A.: Deformation behavior of open-cell dry natural rubber foam: Effect
915 of different concentration of blowing agent and compression strain rate. In *AIP Conference Proceedings*, 1835,
916 No. 1, 020007, AIP Publishing LLC, 2017.

917 Schmatz, J., Klaver, J., Jiang, M. and Urai, J.L.: Nanoscale morphology of brine/oil/mineral contacts in connected
918 pores of carbonate reservoirs: Insights on wettability from Cryo-BIB-SEM. *SPE Journal*, 22(05), 1374-1384,
919 <https://doi.org/10.2118/180049-PA>, 2017.

920 Schneider, J., Flemings, P.B., Day-Stirrat, R.J. and Germaine, J.T.: Insights into pore-scale controls on mudstone
921 permeability through resedimentation experiments. *Geology*, 39(11), 1011-1014,
922 <https://doi.org/10.1130/G32475.1> , 2011.

923 Sintubin, M.: Clay fabrics in relation to the burial history of shales. *Sedimentology*, 41(6), 1161-1169,
924 <https://doi.org/10.1130/G32475.1>, 1994.

925 Terzaghi, K. and Peck, R.B.: *Soil Mechanics. Engineering Practice*. John Wiley and Sons, Inc., New York, 1948.

926 Torres, M. E., Milliken, K. L., A. Hüpers, J. H. Kim, S. G. Lee: Authigenic clays versus carbonate formation as
927 products of marine silicate weathering in the input sequence to the Sumatra Subduction Zone, *Gechemistry,*
928 *Geophysics Geosystems*, 23 (4), <https://doi.org/10.1029/2022GC010338>, 2022.

929 Ukar, E. and Cloos, M.: Cataclastic deformation and metasomatism in the subduction zone of mafic blocks-in-
930 mélange, San Simeon, California, *Lithos*, 346, 105116, <https://doi.org/10.1016/j.lithos.2019.06.018>, 2019.

931 Vasseur, G., Djeran-Maigre, I., Grunberger, D., Rousset, G., Tessier, D. and Velde, B.: Evolution of structural and
932 physical parameters of clays during experimental compaction, *Marine and petroleum geology*, 12(8), pp.941-954,
933 [https://doi.org/10.1016/0264-8172\(95\)98857-2](https://doi.org/10.1016/0264-8172(95)98857-2), 1995.

934 Velde, B.: Compaction trends of clay-rich deep sea sediments, *Marine Geology* 133(3-4): 193-201,
935 [https://doi.org/10.1016/0025-3227\(96\)00020-5](https://doi.org/10.1016/0025-3227(96)00020-5), 1996.

936 Vrolijk, P.: On the mechanical role of smectite in subduction zones. *Geology*, 18(8), pp.703-707,
937 [https://doi.org/10.1130/0091-7613\(1990\)018<0703:OTMROS>2.3.CO;2](https://doi.org/10.1130/0091-7613(1990)018<0703:OTMROS>2.3.CO;2), 1990.

938 Wang, X., Jiang, Z., Jiang, S., Chang, J., Zhu, L., Li, X. and Li, J.: Full-scale pore structure and fractal dimension
939 of the Longmaxi shale from the Southern Sichuan Basin: Investigations using FE-SEM, gas adsorption and
940 mercury intrusion porosimetry. *Minerals*, 9(9), p.543, <https://doi.org/10.3390/min9090543>, 2019.

941 Yagiz, S.: Overview of classification and engineering properties of shales for design considerations.
942 In *Construction and Materials Issues* 2001, 156-165, 2001.

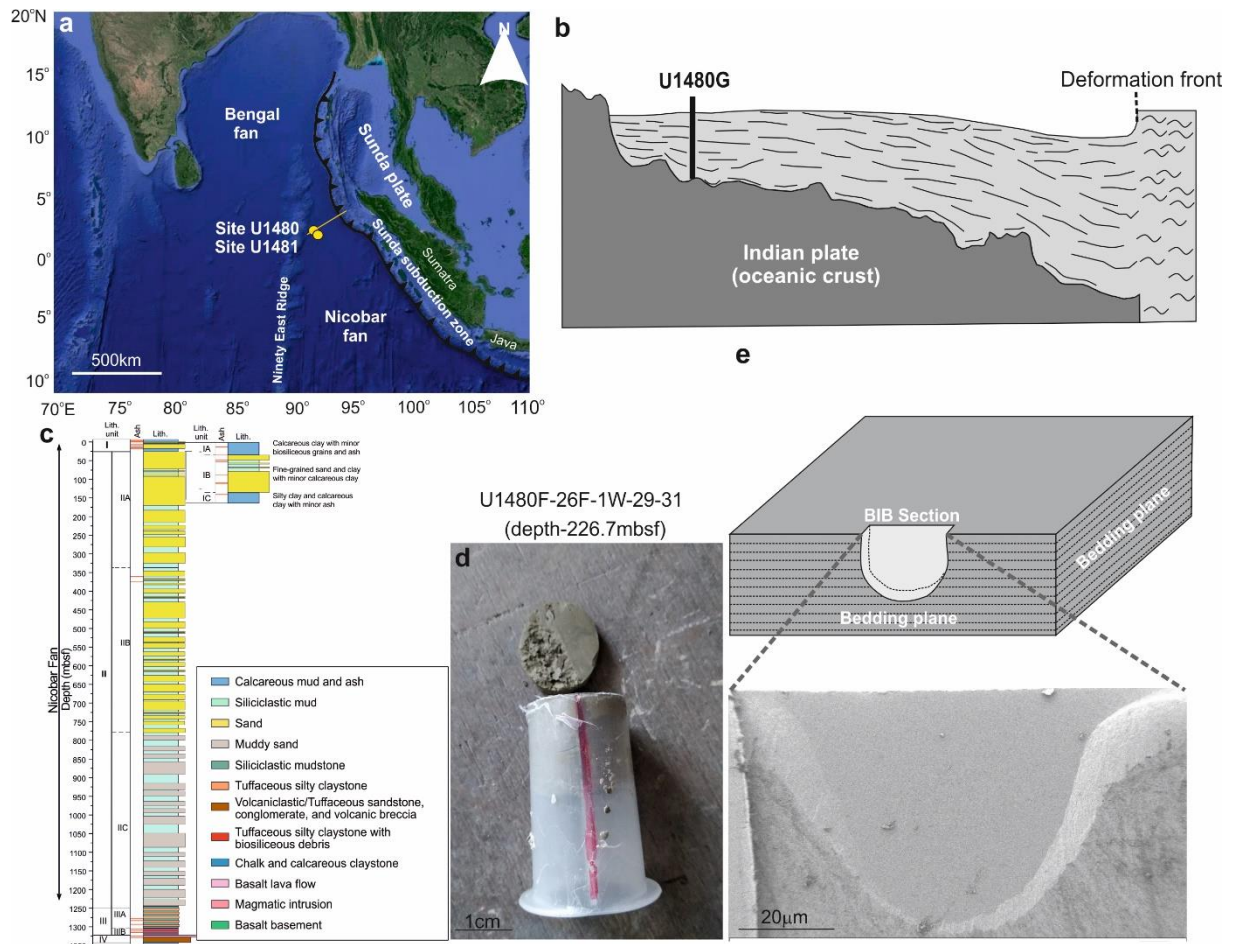
943 Zakaria, Z., Mohamad Ariff, Z. and Abu Bakar, A.: Monitoring deformation mechanism of foam cells in
944 polyethylene foams via optical microscopy: Effect of density and microstructure. *Journal of Cellular*
945 *Plastics*, 54(6), 957-976, <https://doi.org/10.1177/0021955X18795035>, 2018.

946 Zhou, J., Shrotriya, P. and Soboyejo, W.O.: Mechanisms and mechanics of compressive deformation in open-cell
947 Al foams. *Mechanics of Materials*, 36(8), 781-797, <https://doi.org/10.1016/j.mechmat.2003.05.004>, 2004.

948

949

950



951

952 **Fig.1:** (a) **Satellite image** of Sumatra subduction zone and location of U1480 and U1481 drilling sites (created
 953 from Google Maps). (b) **Schematic diagram showing location of primary drilling site and deepest drill hole (Hole**
 954 **G) at site U1480 in sectional view** (adapted from seismic profile after Hüpers et al., 2017). **Location and extension**
 955 **of the seismic profile is represented by red line in (a).** (c) Lithostratigraphic units encountered at Site U1480
 956 (adapted after McNeill et al., 2017). (d) Representative tube sample received from IODP repository, Japan. Red-
 957 colored line on tube surface represents notch used to denote orientation of samples collected from drill core. (e)
 958 Representative BIB cross-section polished perpendicular to bedding planes.

959

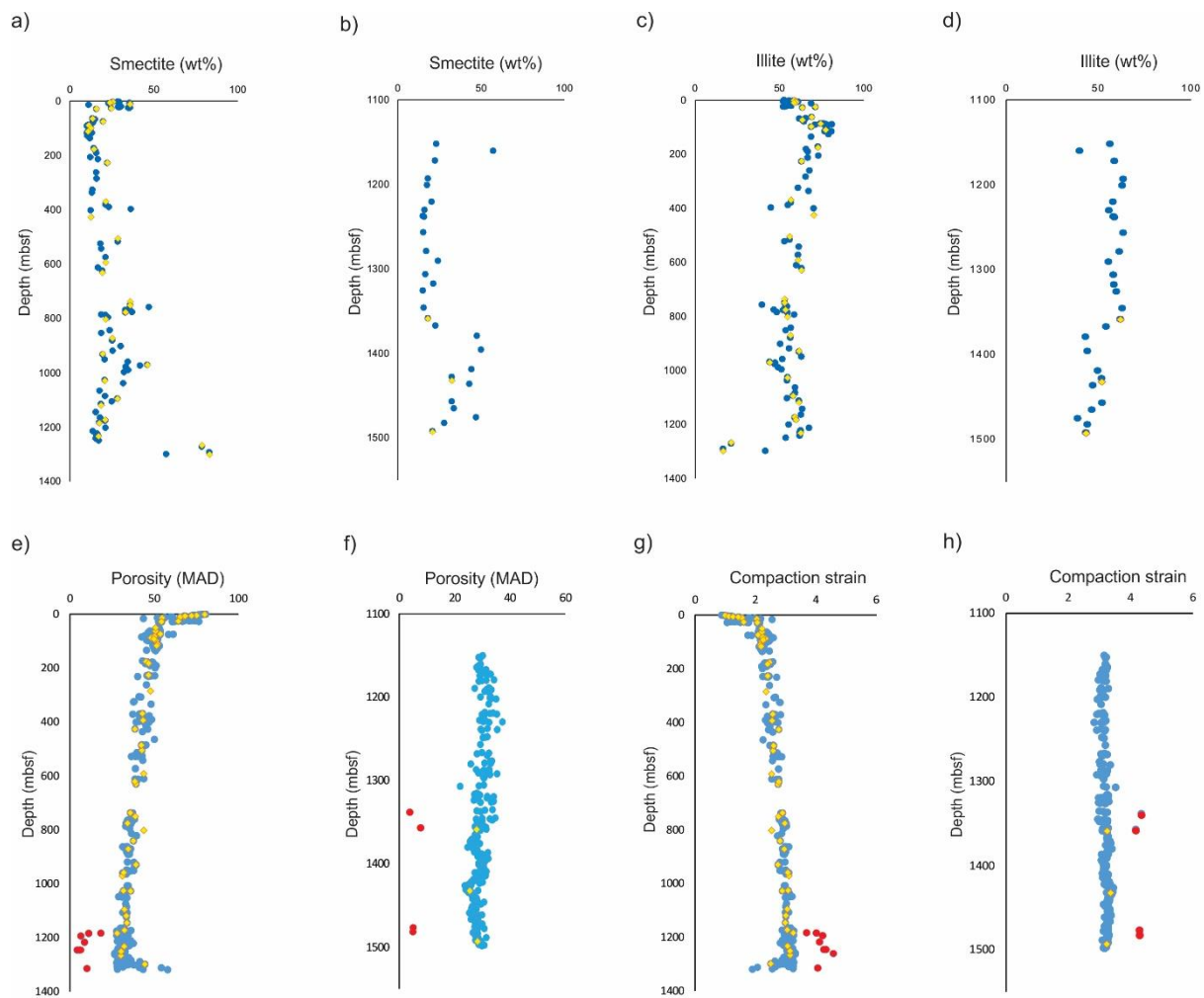
960

961

962

963

964



965

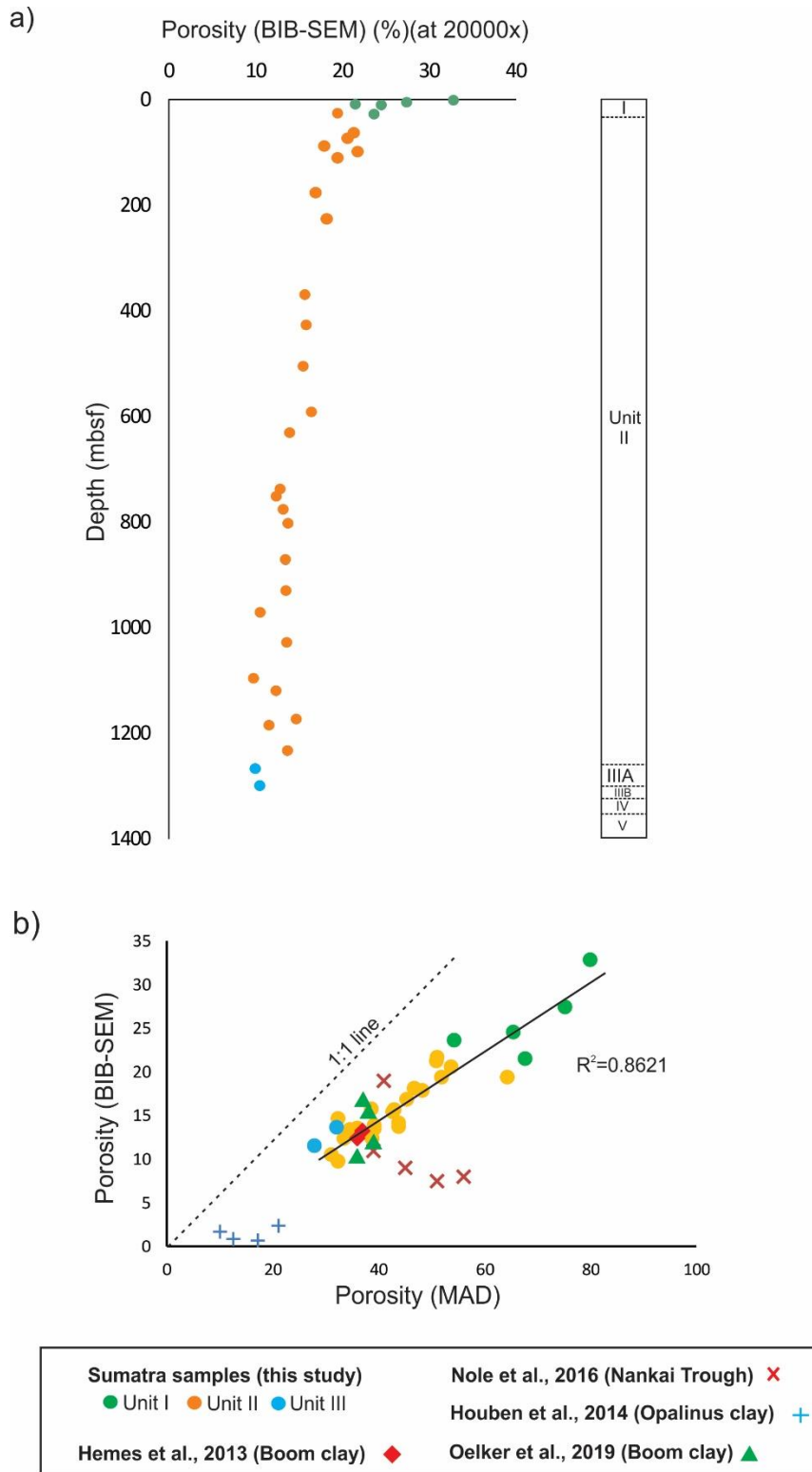
966 **Fig.2:** Depth profiles of smectite content (wt%; clay fraction) for Sites U1480 (a) and U1481 (b) (blue symbol).
 967 Depth profiles of illite content (wt%; clay fraction) for Sites U1480 (a) and U1481 (b) (blue symbol). Yellow
 968 symbols indicate samples analyzed by SEM imaging. (e) and (f) Shipboard MAD (Moisture and density) porosity
 969 profiles for mudstone samples recovered from Sites U1480 and U1481 (blue symbol). (g) and (h) Calculated
 970 compaction strain profiles for Sites U1480 and U1481 (blue symbols). Red-colored points are cemented
 971 (concretion) samples. Clay mineralogy data plotted from Rosenberger et al. (2020), and MAD data extracted from
 972 McNeill et al. (2017).

973

974

975

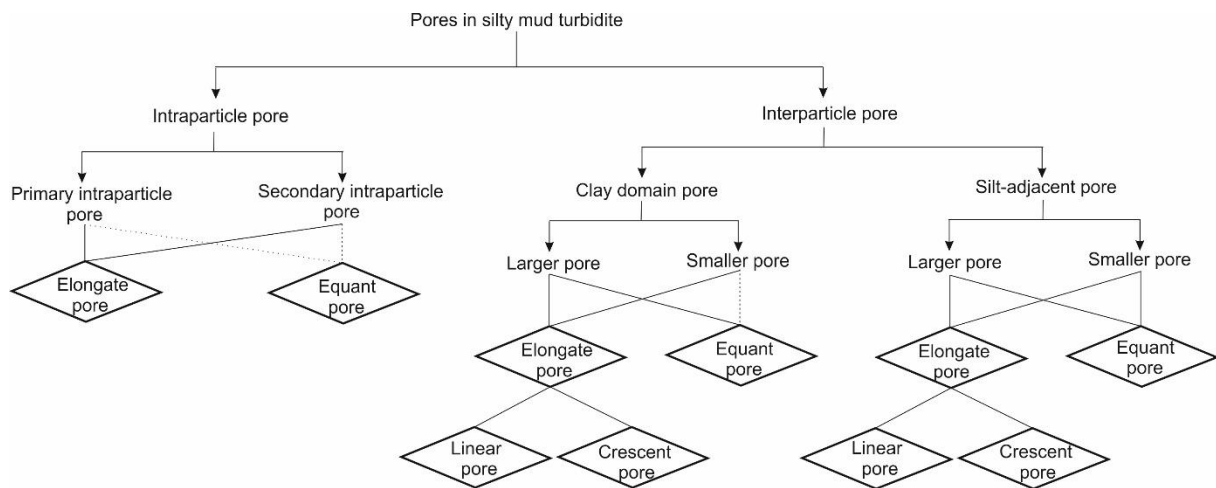
976



977 **Fig.3:** Porosity data for Units I (green dots), II (orange dots), and IIIA (blue dots). (a) BIB-SEM porosity - depth
 978 plot, (b) BIB-SEM porosity vs MAD porosity. Note: linear relationship that intersects origin. Data reported by
 979 Hemes et al. (2013); Houben et al. (2014); and Oelker et al. (2019) follow similar trend. However, data estimated
 980 from Nole et al. (2016) deviates from trend.

981

982



983

984

985 **Fig.4:** Classification scheme adopted to demonstrate pore reduction mechanics with increasing compactional
986 strain. Dashed lines indicate rare pore types.

987

988

989

990

991

992

993

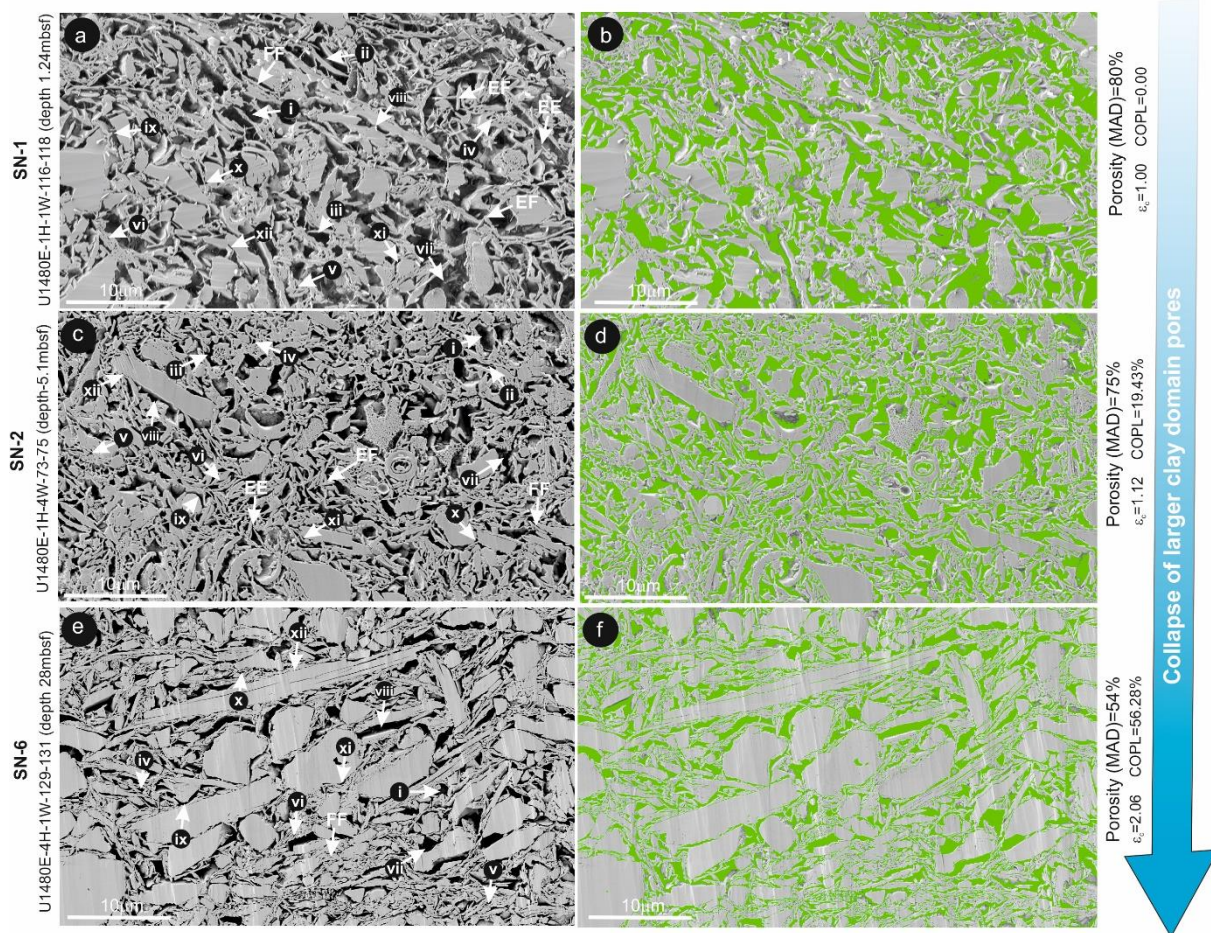
994

995

996

997

998



999

1000 **Fig.5:** Microstructural overview (BIB-SEM) of samples SN-1 (a and b), SN-2 (c and d), and SN-6 (e and f). Green
 1001 color represents segmented pores of the corresponding microstructure of sample. i = Equant large clay domain
 1002 pores, ii = elongated large clay domain pores, iii = Crescent-shaped large clay domain pores, iv = equant small
 1003 clay domain pores, v = Crescent-shaped small clay domain pores, vi = elongated small clay domain pores, vii =
 1004 Equant large silt-adjacent pores, viii = elongated large silt-adjacent pores, ix = Crescent-shaped large silt-adjacent
 1005 pores, x = equant small silt-adjacent pores, xi = Crescent-shaped small silt-adjacent pores, xii = elongated small
 1006 silt-adjacent pores. **EE= Edge to edge contact, EF=Edge to face contact, and FF=Face to face contact.**

1007

1008

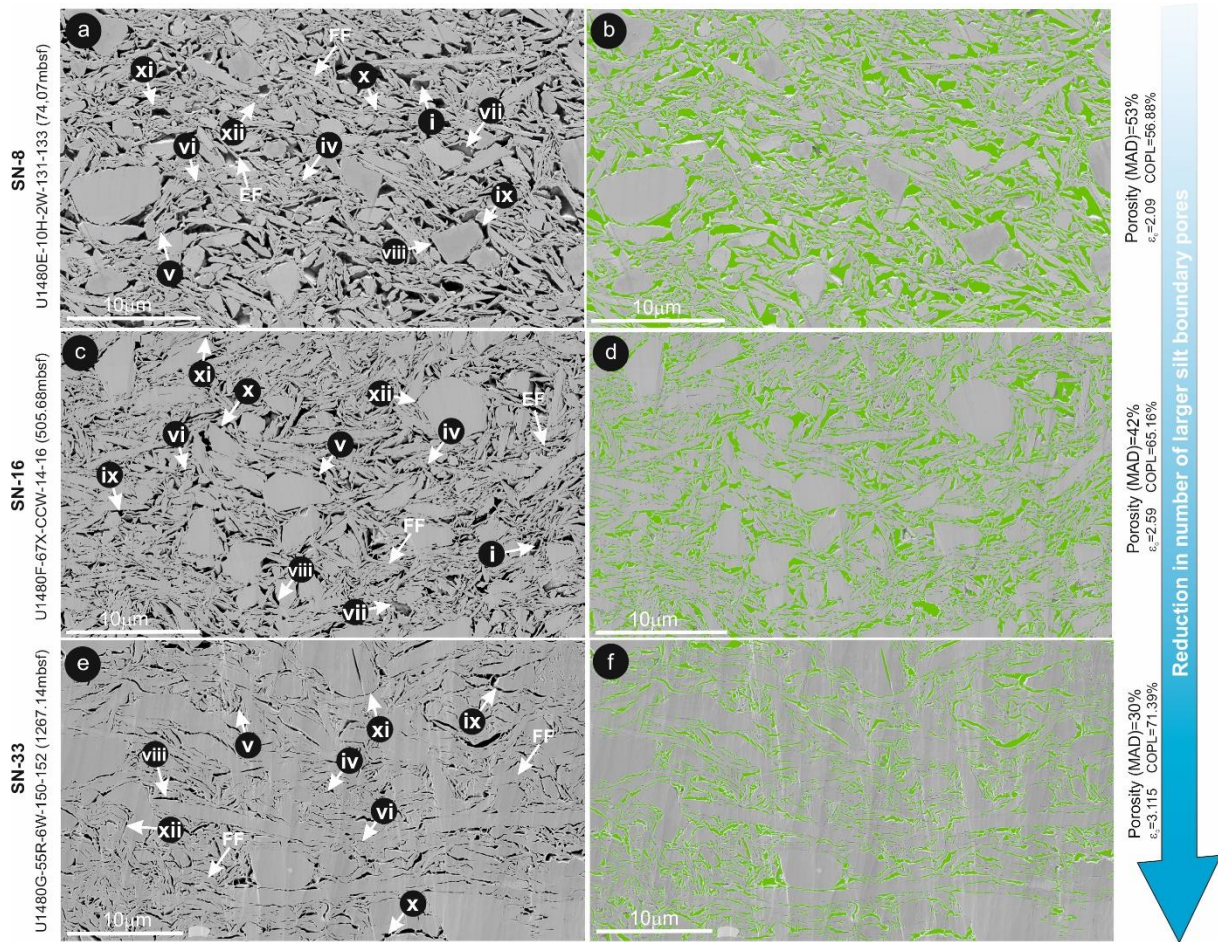
1009

1010

1011

1012

1013



1014

1015 **Fig.6:** Microstructural overview (BIB-SEM) of samples SN-8 (a and b), SN-16 (c and d), and SN-32 (e and f).
 1016 Green color represents segmented pores of the corresponding microstructure of sample. i = Equant large clay
 1017 domain pores, ii = elongated large clay domain pores, iii = Crescent-shaped large clay domain pores, iv = equant
 1018 small clay domain pores, v = Crescent-shaped small clay domain pores, vi = elongated small clay domain pores,
 1019 vii = Equant large silt-adjacent pores, viii = elongated large silt-adjacent pores, ix = Crescent-shaped large silt-
 1020 adjacent pores, x = equant small silt-adjacent pores, xi = Crescent-shaped small silt-adjacent pores, xii = elongated
 1021 small silt-adjacent pores. **FF= Face to face contact, EF= Edge to face contact.**

1022

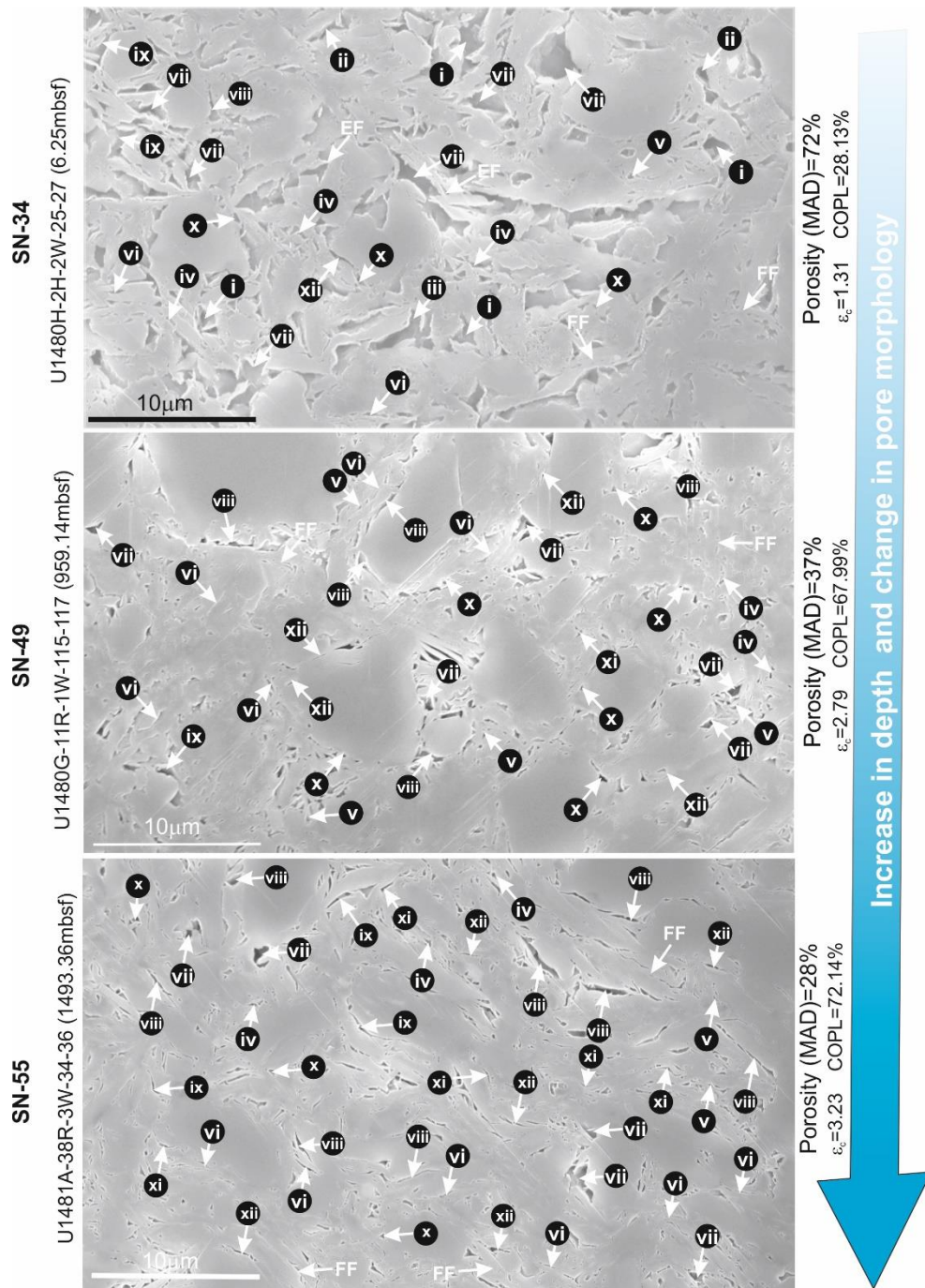
1023

1024

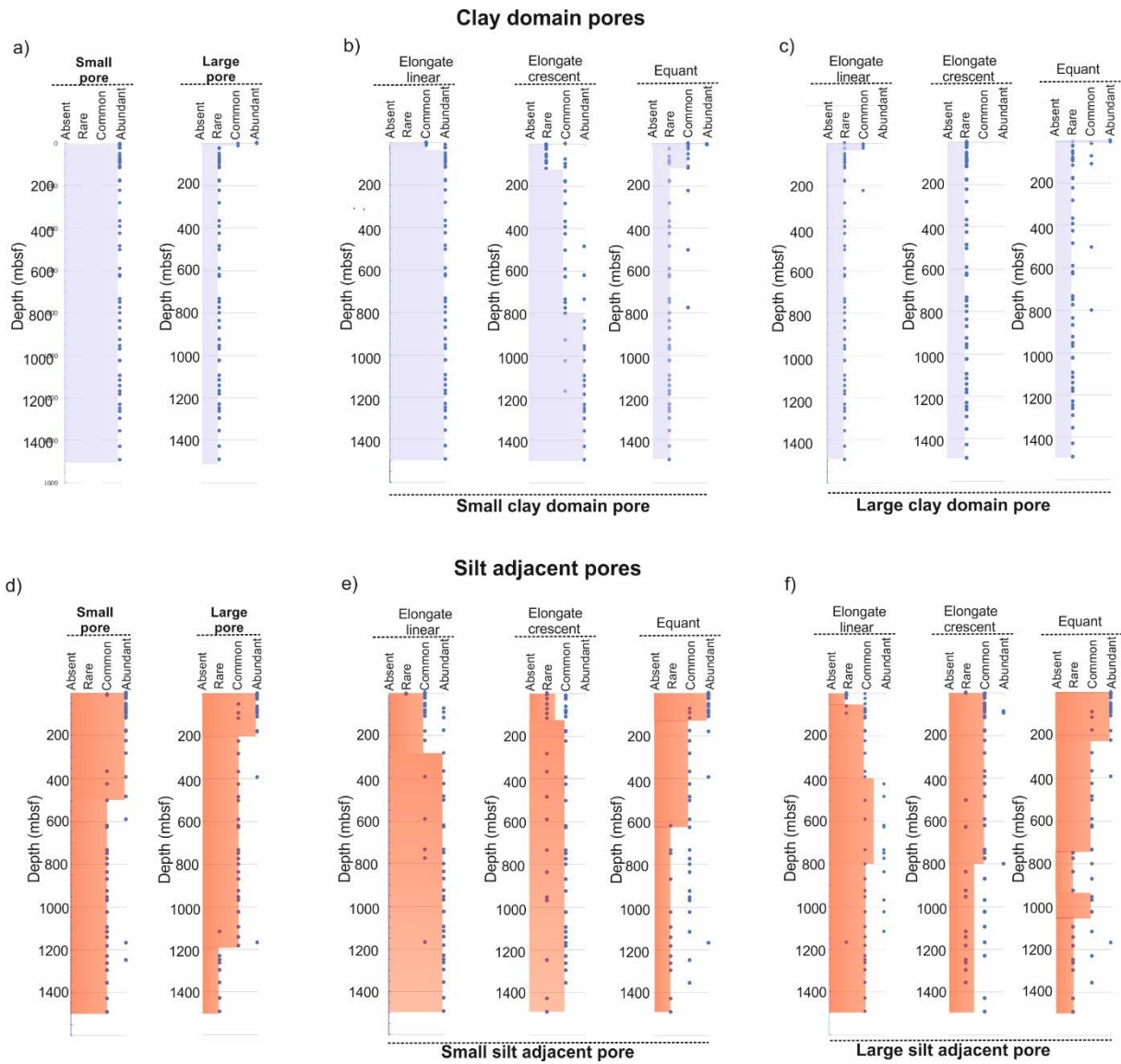
1025

1026

1027



1030 **Fig.7:** Microstructural overview (Field Emission SEM) of samples SN-34, SN-49, and SN-55. i = Equant large
 1031 clay domain pores, ii = elongated large clay domain pores, iii = Crescent-shaped large clay domain pores, iv =
 1032 equant small clay domain pores, v = Crescent-shaped small clay domain pores, vi = elongated small clay domain
 1033 pores, vii = Equant large silt-adjacent pores, viii = elongated large silt-adjacent pores, ix = Crescent-shaped large
 1034 silt-adjacent pores, x = equant small silt-adjacent pores, xi = Crescent-shaped small silt-adjacent pores, xii =
 1035 elongated small silt-adjacent pores. **FF= Face to face contact, EF= Edge to face contact.**



1037

1038 **Fig.8:** Pore type summary for clay domain (a-c) and silt-adjacent (d-f) pore types. (a) abundance of small and large
 1039 clay domain pores; (b) and (c) depth progression of small and large clay domain pore morphologies; (d) abundance
 1040 of small and large silt-adjacent pores; (e) and (f) depth progression of small and large clay domain pore
 1041 morphologies. Abundant = >25% pores, common = 2%-25% pores, rare = 0-2% pores, absent = not observed.

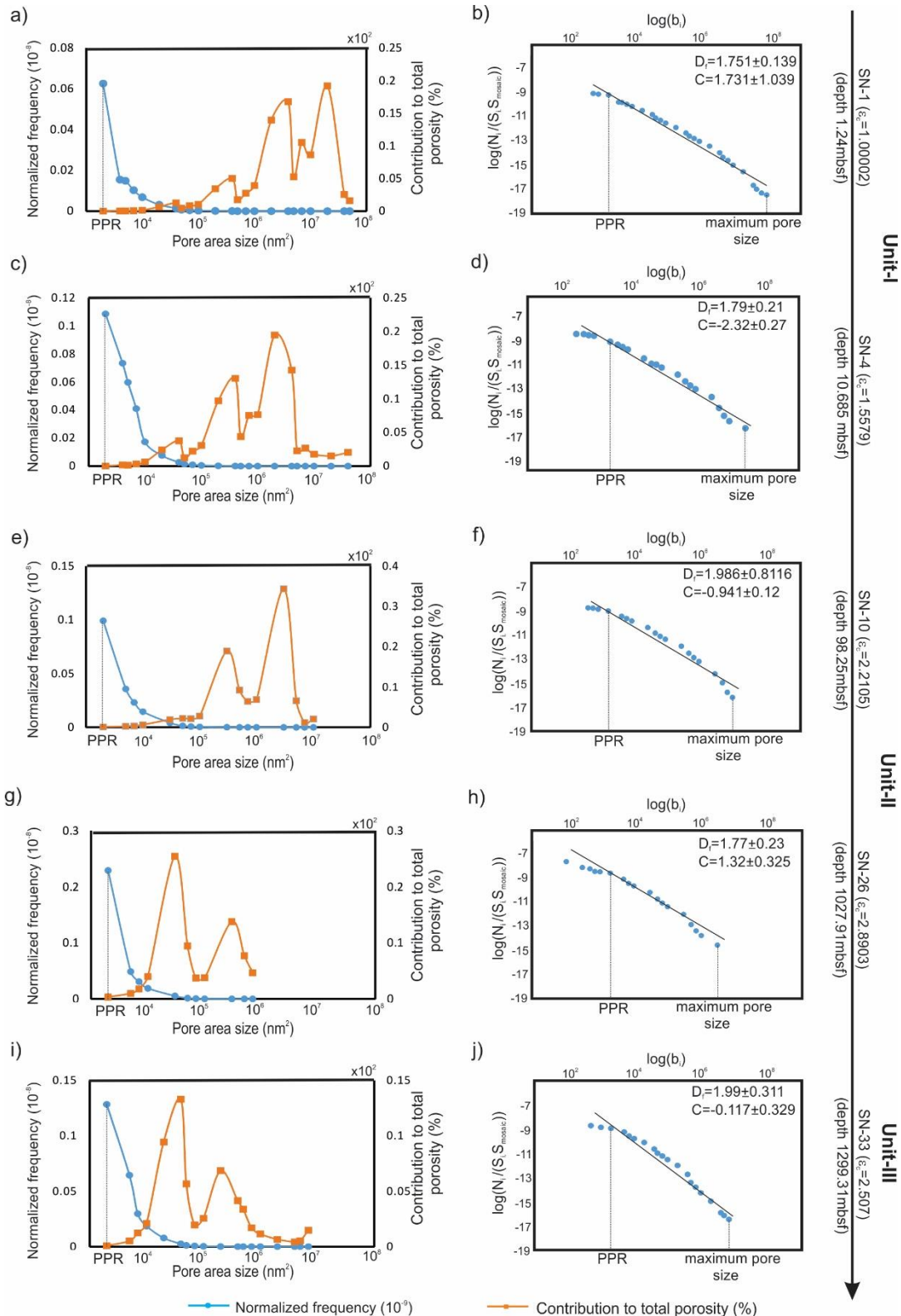
1042

1043

1044

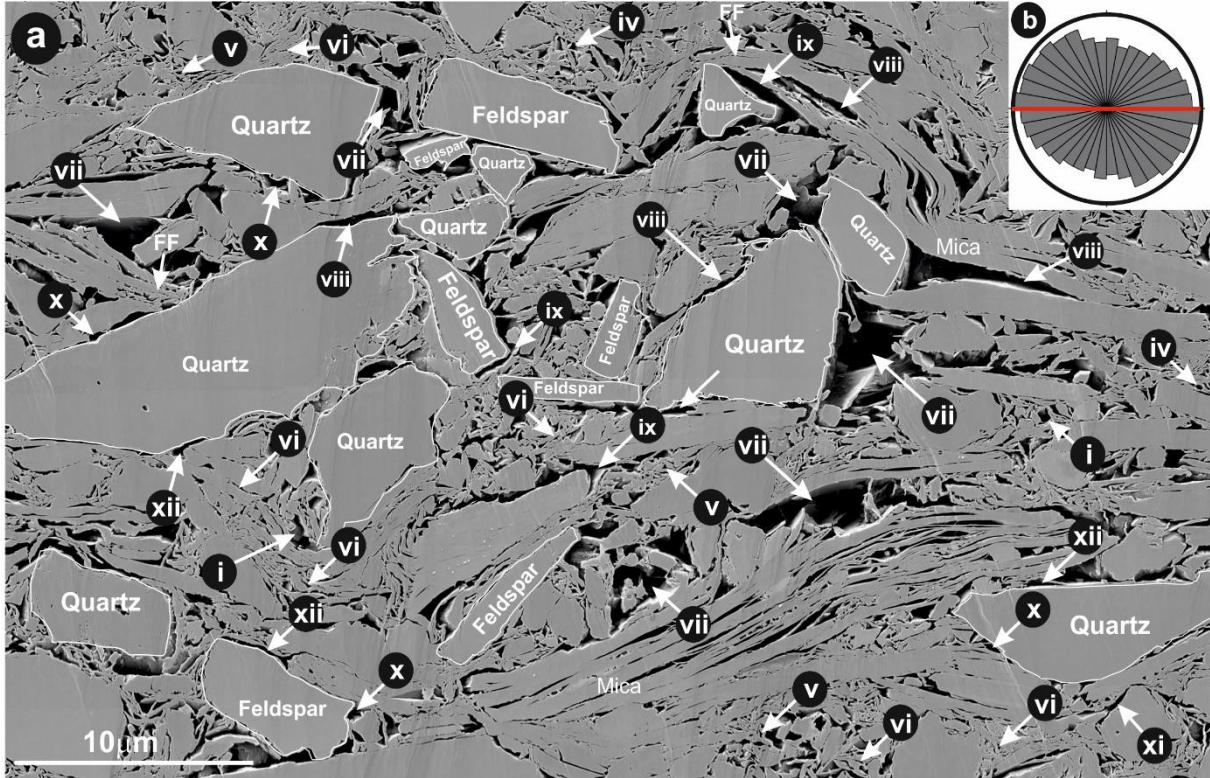
1045

1046



1048 **Fig.9:** Pore size distribution defined by pore area. Left column: normalized frequency (blue) and contribution to
 1049 total porosity (orange). Right column: pore size-frequency log-log distribution. Power-law between PPR and
 1050 maximum pore size interpreted as black line with corresponding regression parameters. Sample number, depth,
 1051 and compaction strain defined along right side of diagram

SN- 29 (U1480G-45R-1W-93-95, depth 1172.88mbsf)



1053

1054

1055 **Fig.10:** Silt-rich sample (SN-29; 1173 mbsf) (a) i = Equant large clay domain pores, ii =elongated large clay
1056 domain pores, iii = Crescent-shaped large clay domain pores, iv = equant small clay domain pores, v = Crescent-
1057 shaped small clay domain pores, vi = elongated small clay domain pores, vii = Equant large silt-adjacent pores,
1058 viii = elongated large silt-adjacent pores, ix = Crescent-shaped large silt-adjacent pores, x =equant small silt-
1059 adjacent pores, xi = Crescent-shaped small silt-adjacent pores, xii = elongated small silt-adjacent pores.(b) Rose
1060 diagram of long axes of pores (bedding = red line). **FF= face to face contact of clay particles.**

1061

1062

1063

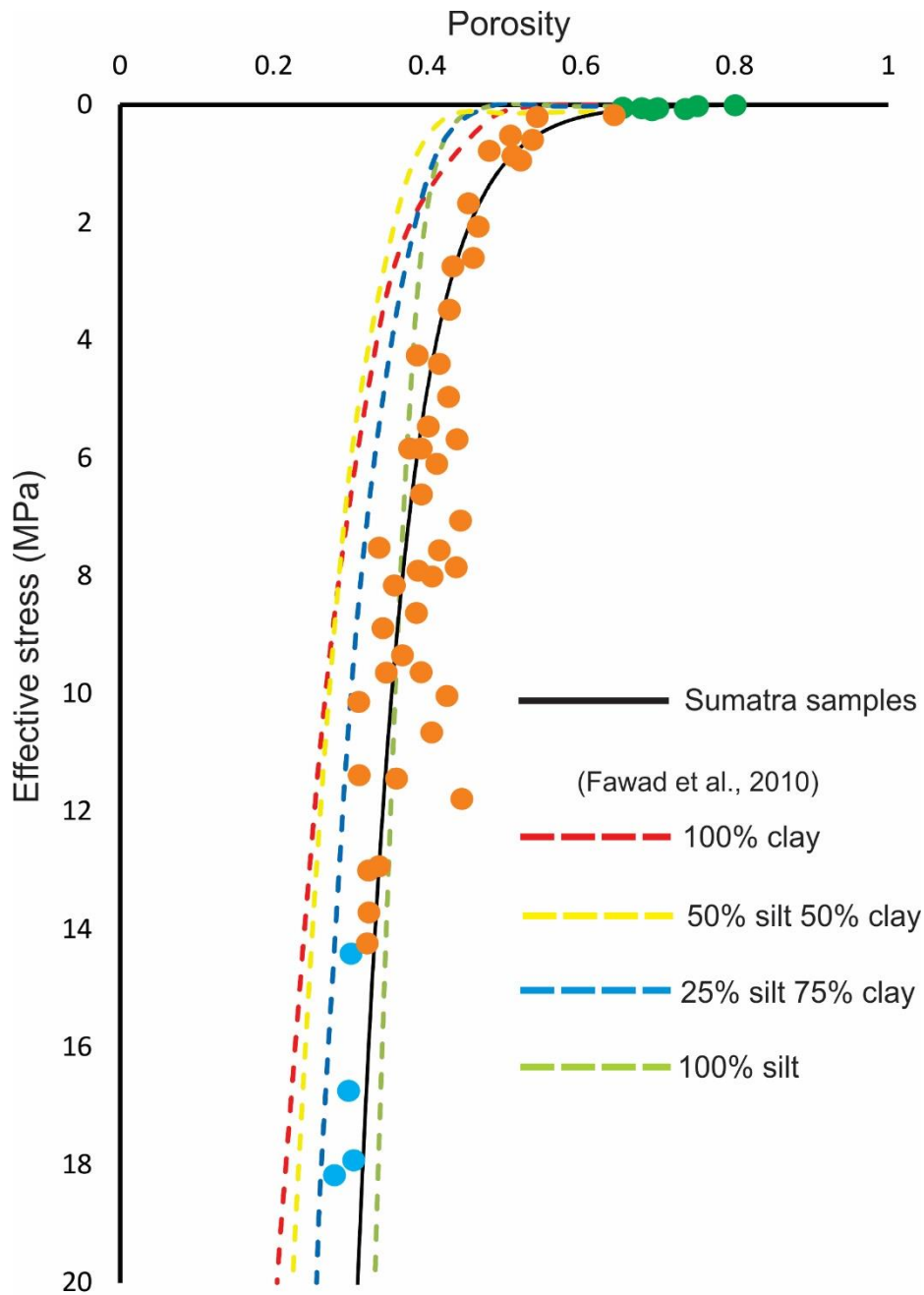
1064

1065

1066

1067

1068



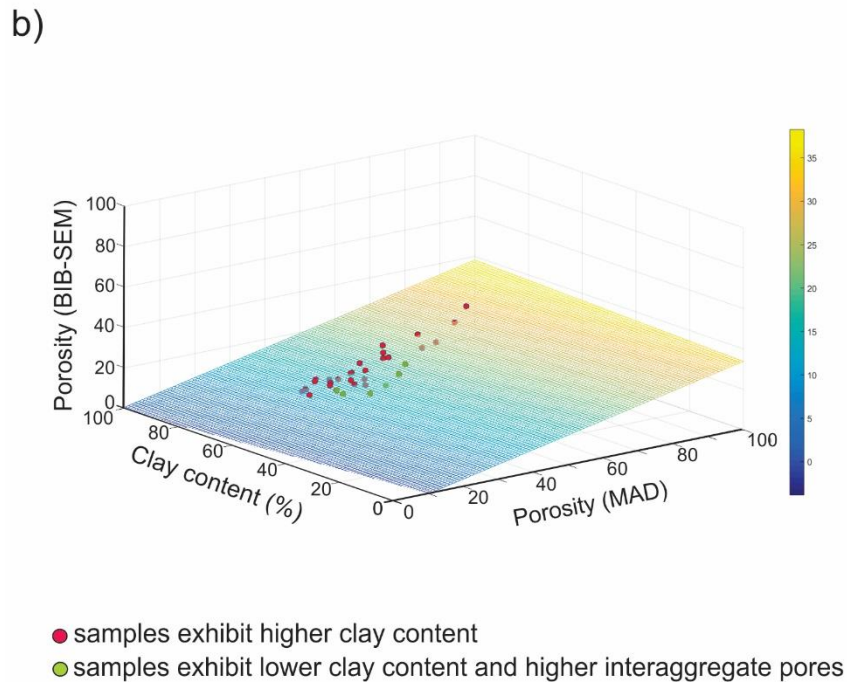
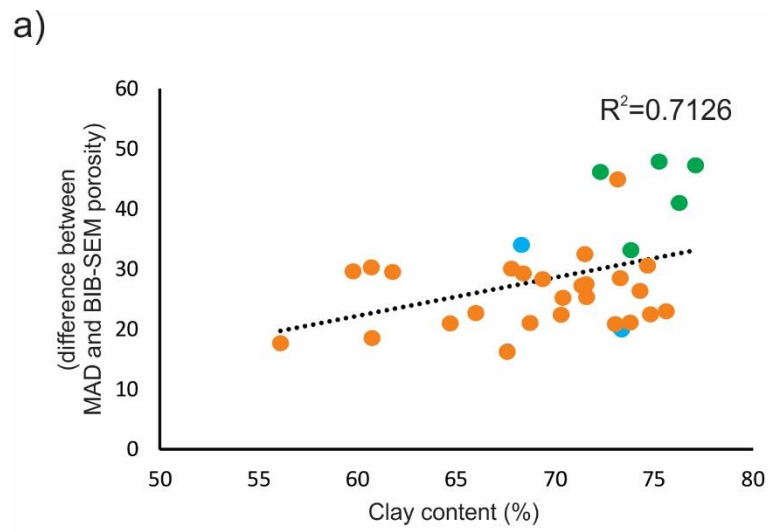
1070

1071 **Fig.11:** Effective stress vs porosity (MAD) for experimental mixtures of clay and silt (dashed lines; Fawad et al.,
 1072 2010) compared with Sumatra data (Unit 1 = green; Unit II = orange; Unit III = blue). Solid black solid line is a
 1073 best-fit data regression for Sumatra samples.

1074

1075

1076



1078

1079 **Fig.12:** (a) Clay content vs difference between MAD and BIB-SEM porosity. (b) Multivariate regression
 1080 analysis using three parameters: BIB-SEM porosity, clay content, and MAD porosity (33 samples).

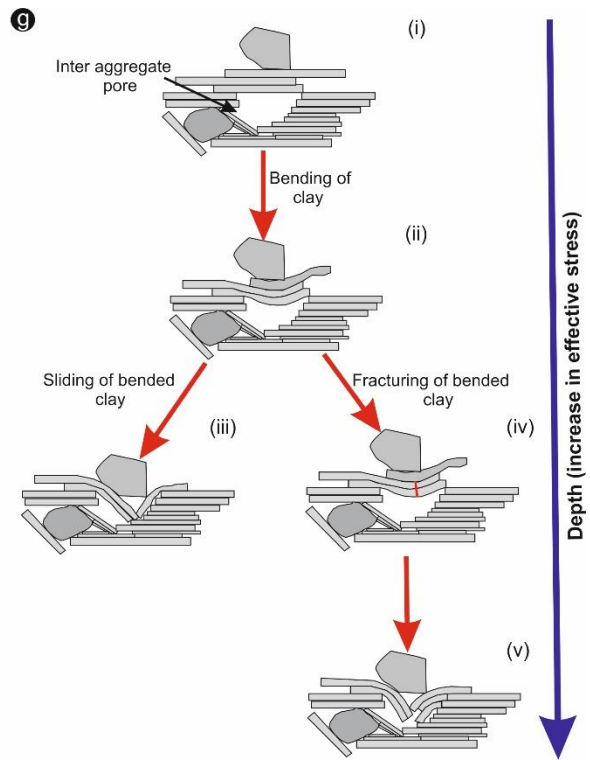
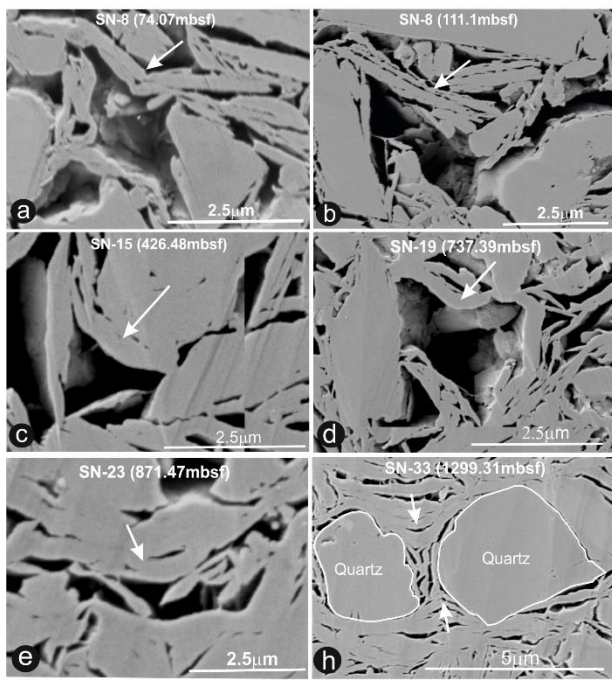
1081

1082

1083

1084

1085



1086

1087 **Fig.13:** a-f: examples of bent clay particles on top of silt-adjacent larger pores; sample ID and depth labelled on
1088 photos. (g) Micromechanical model for collapse of large silt-adjacent pores.

1089

1090

1091

1092

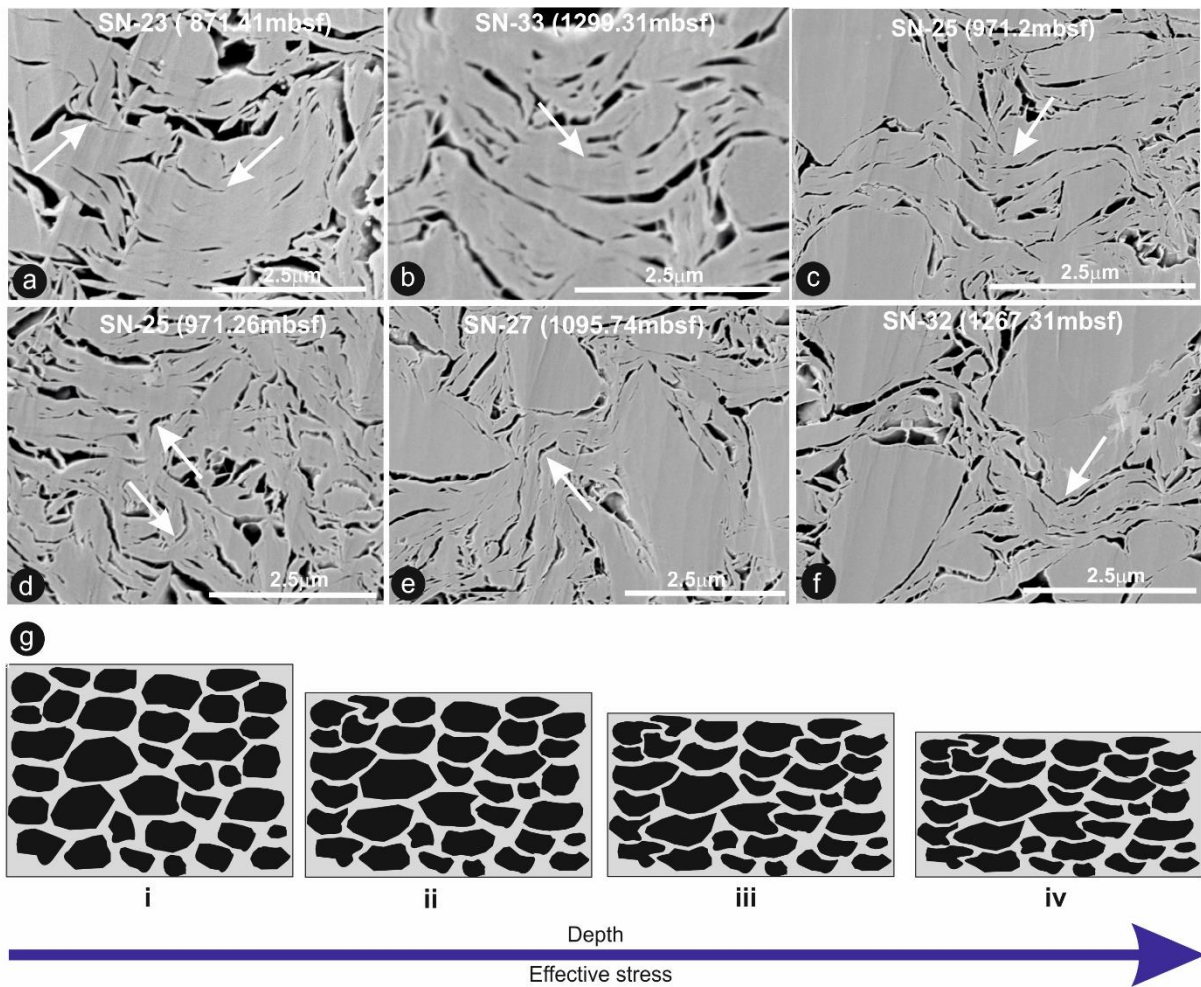
1093

1094

1095

1096

1097



1098

1099 **Fig.14:** a-f: examples of clay aggregate bending (white arrows). (g) Conceptual diagram tracing porosity reduction
 1100 and increase in preferred alignment of the long axes of pores by bending of clay perpendicular to applied vertical
 1101 stress.

1102

1103

Table 1: Core description, bulk mineralogy (McNeill et al., 2017) and clay composition (Rosenberger et al., 2020) of the analysed samples.

	Sample no	Site	Hole	Core	Type	Sec	Depth	Unit	Bulk mineralogical comp (XRD)					Clay mineralogical comp (XRD)			
									Total clay	Quartz	Plag.	Calc.	Pc/pc+ _g	Smect.	Illite	Chl+Kaol	Quartz
First set of sample (Analysed at Aachen university)	SN-1	U1480	E	1	H	1	1.24	I	68.84	11.53	9.20	10.4	0.44	25.40	58.60	9.10	6.90
	SN-2	U1480	E	1	H	4	5.10	I	67.52	12.14	8.90	11.4	0.42	23.70	60.00	12.30	4.00
	SN-3	U1480	E	2	H	1	9.18	I	70.99	15.27	12.10	1.64	0.44	37.59	48.79	10.77	2.85
	SN-4	U1480	E	2	H	2	10.69	I	65.85	15.19	10.32	8.64	0.40	35.80	58.80	3.10	2.30
	SN-5	U1480	E	3	H	6	26.05	I	61.89	19.04	11.72	7.35	0.38	40.09	43.35	13.29	3.27
	SN-6	U1480	E	4	H	1	28.00	IIA	63.45	21.13	12.94	2.47	0.38	13.73	61.64	10.80	13.83
	SN-7	U1480	E	9	H	2	63.24	IIA	64.47	19.59	12.67	3.26	0.39	11.02	67.04	15.44	6.50
	SN-8	U1480	E	10	H	2	74.07	IIA	64.97	19.70	12.13	3.20	0.38	20.87	58.32	11.85	8.96
	SN-9	U1480	E	11	H	5	87.98	IIA	60.48	20.71	16.53	2.27	0.44	6.29	73.86	10.06	9.79
	SN-10	U1480	F	2	H	1	98.25	IIA	63.84	18.51	15.57	2.07	0.46	7.17	76.60	11.81	4.42
	SN-11	U1480	F	3	H	3	111.10	IIA	67.18	16.42	14.35	2.05	0.47	6.10	76.22	11.12	6.56
	SN-12	U1480	F	15	F	2	176.50	IIA	62.52	21.59	13.95	1.94	0.39	12.56	69.03	16.08	2.34
	SN-13	U1480	F	26	F	1	226.70	IIA	70.27	16.56	11.63	1.53	0.41	22.16	57.52	17.84	2.49
	SN-14	U1480	F	53	X	2	369.19	IIB	68.80	18.18	11.60	1.43	0.39	21.15	52.78	22.79	3.29
	SN-15	U1480	F	59	X	1	426.68	IIB	68.66	17.49	10.50	3.35	0.38	9.25	69.20	13.00	8.55
	SN-16	U1480	F	67	X	CC	505.32	IIB	70.86	16.95	10.99	1.20	0.39	30.19	49.18	14.12	6.50
	SN-17	U1480	F	76	X	1	592.42	IIB	61.63	23.74	12.11	2.52	0.34	22.20	55.64	16.98	5.18
	SN-18	U1480	F	80	X	CC	630.55	IIB	68.76	15.16	13.81	2.27	0.35	18.96	58.58	18.81	3.65
	SN-19	U1480	F	91	X	1	737.39	IIB	67.85	18.93	11.86	1.35	0.39	36.05	45.70	13.83	4.43
	SN-20	U1480	F	92	X	1	751.16	IIB	67.78	19.32	11.75	1.15	0.38	36.05	45.70	13.83	4.43
	SN-21	U1480	G	4	R	2	776.17	IIB	69.70	18.21	12.09	0.00	0.40	39.70	39.45	13.27	7.58
	SN-22	U1480	G	7	R	CC	802.55	IIC	62.30	22.44	13.62	1.64	0.38	23.42	53.62	19.97	2.99
	SN-23	U1480	G	14	R	2	871.87	IIC	66.07	20.41	12.14	1.38	0.37	28.17	49.85	18.04	3.93
	SN-24	U1480	G	20	R	1	929.81	IIC	67.28	18.26	11.84	2.61	0.39	20.60	56.66	17.85	4.90
	SN-25	U1480	G	24	R	3	971.26	IIC	66.44	19.30	13.23	1.03	0.37	41.36	40.43	14.16	4.05
	SN-26	U1480	G	30	R	2	1027.91	IIC	65.18	21.99	12.83	0.00	0.37	21.39	50.89	24.40	3.32
	SN-27	U1480	G	37	R	2	1095.74	IIC	68.14	18.34	11.68	1.84	0.39	30.15	50.76	15.03	4.06
	SN-28	U1480	G	41	R	1	1119.70	IIC	69.60	15.67	11.28	3.45	0.42	19.11	57.36	19.38	4.16
	SN-29	U1480	G	45	R	1	1172.88	IIC	63.40	21.21	11.36	5.03	0.41	22.26	54.12	20.25	3.37
	SN-30	U1480	G	46	R	3	1184.39	IIC	65.75	17.80	11.04	5.40	0.38	17.55	56.58	21.04	4.83
	SN-31	U1480	G	51	R	CC	1233.15	IIC	61.85	22.34	11.94	3.87	0.35	16.88	58.90	19.40	4.82
	SN-32	U1480	G	55	R	6	1267.14	IIIA	68.04	18.55	11.96	1.46	0.39	63.71	24.68	0.03	11.58
	SN-33	U1480	G	59	R	1	1299.31	IIIA	72.12	15.47	12.41	0.00	0.69	54.45	36.44	2.64	6.47
Second set of sample (Analysed at BEG)	SN-34	U1480	H	2	H	2	6.25	IB	71.41	17.89	10.70	0.00	0.37	24.97	53.79	19.40	1.85
	SN-35	U1480	E	1	H	6	7.21	IB	70.10	11.83	10.44	7.63	0.47	24.03	54.95	19.32	1.70
	SN-36	U1480	H	3	H	1	14.28	IB	62.21	20.57	14.34	2.88	0.41	5.22	70.27	9.24	15.27
	SN-37	U1480	E	4	H	1	28.12	IIA	63.45	21.13	12.94	2.47	0.38	13.73	61.64	10.80	13.83
	SN-38	U1480	E	7	H	1	50.82	IIA	61.20	22.04	14.09	2.67	0.39	11.02	67.04	15.44	6.50
	SN-39	U1480	H	10	H	2	83.02	IIA	59.31	21.08	15.48	4.14	0.42	6.29	73.86	10.06	9.79
	SN-40	U1480	H	16	H	1	117.13	IIA	62.22	20.06	15.56	2.17	0.44	11.93	72.73	10.55	4.79
	SN-41	U1480	E	12	H	2	92.82	IIA	59.39	22.78	15.75	2.08	0.41	6.11	71.56	9.49	12.84
	SN-42	U1480	F	16	F	3	182.62	IIA	64.16	20.84	12.83	2.17	0.38	13.68	63.09	16.46	6.76
	SN-43	U1480	F	37	X	2	285.51	IIA	66.51	20.24	11.54	1.71	0.36	14.72	62.33	19.07	3.88
	SN-44	U1480	F	55	X	5	394.01	IIB	58.39	28.27	13.35	0.00	0.32	39.89	37.88	12.81	9.41
	SN-45	U1480	F	65	X	CC	486.72	IIB	59.06	25.70	13.85	1.39	0.35	30.19	49.18	14.12	6.50
	SN-46	U1480	F	79	X	1	621.2	IIB	66.89	18.95	12.55	1.61	0.40	18.96	58.58	18.81	3.65
	SN-47	U1480	F	91	X	1	737.47	IIB	67.85	18.93	11.86	1.35	0.39	36.05	45.70	13.83	4.43
	SN-48	U1480	G	11	R	1	841.56	IIC	63.6	22.2	12.5	1.80	0.36	26.26	50.81	19.37	3.57
	SN-49	U1480	G	23	R	1	959.15	IIC	58.32	26.19	13.52	1.97	0.34	33.19	46.20	17.84	2.78
	SN-50	U1480	G	30	R	1	1026.34	IIC	68.49	17.73	12.05	1.73	0.40	21.39	50.89	24.40	3.32
	SN-51	U1480	G	42	R	3	1145.91	IIC	60.53	21.80	12.46	5.21	0.36	13.56	61.43	17.58	7.44
	SN-52	U1480	G	54	R	2	1251.5	IIIA	63.2	22.41	13.18	1.17	0.37	15.66	52.66	15.92	15.76
	SN-53	U1481	A	23	R	5	1358.9	IIC	68.6	16.90	11.07	3.36	0.40	18.08	57.77	19.98	4.17
	SN-54	U1481	A	32	R	1	1432.5	IIIA	65.5	22.53	10.76	1.19	0.32	32.44	45.82	16.54	5.20
	SN-55	U1481	A	38	R	3	1493.3	IIIA	60.5	25.71	12.79	0.98	0.33	19.90	42.07	13.66	24.37